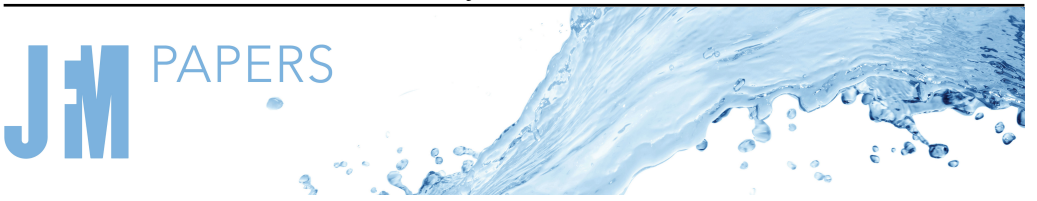
J. Fluid Mech. (2026), *vol.* 1045, A19, doi:10.1017/jfm.2026.12134



Control of axial dispersion in polymeric flows: Magnetic effect versus electro-osmotic effect

Xiaoping Wang[1], **Mengqi Zhang**[2,3] **and Haitao Qi**[4]

[1]Department of Mathematics, Harbin Institute of Technology, Weihai 264209, PR China

[2]Department of Mathematics, City University of Hong Kong, 83 Tat Chee Avenue, Kowloon Tong, Hong Kong, PR China

[3]Department of Mechanical Engineering, National University of Singapore, 9 Engineering Drive 1, Singapore 117575, Republic of Singapore

[4]School of Mathematics and Statistics, Shandong University, Weihai 264209, PR China

Corresponding authors: Haitao Qi, htqi@sdu.edu.cn; Mengqi Zhang, ma.zmq@cityu.edu.hk

(Received 20 November 2025 UTC; revised 30 March 2026 UTC; accepted 3 September 2026 UTC)

Since Taylor's seminal work on the dispersion of soluble matter, the modelling and control of solute dispersion have received considerable attention. This study investigates the solute dispersion in polymer solutions driven by unsteady magnetohydrodynamic (MHD)-oscillatory electro-osmotic flow within a microtube, aiming to reveal the transport mechanisms in complex rheological media through microscale flow. Firstly, based on the Debye–Hückel approximation, analytical solutions for the electric potential and velocity distributions of mixed MHD-electrohydrodynamic flows are rigorously derived. Subsequently, using Sankarasubramanian & Gill's generalised dispersion model (1970 *Proc. R. Soc. Lond. A*, vol. 316, pp. 341–350), mathematical models are developed to systematically investigate the temporal evolution of hydrodynamic dispersion. By investigating the synergistic modulation of electrokinetic and magnetic fields, we identify three distinct flow regimes, namely the electric-field-dominant, competitive transition and magnetic-field-limited regimes, and quantitatively define their boundaries and evolution with the oscillatory Reynolds number Re and Deborah number De, thus allowing accurate flow regime classification. Moreover, a non-monotonic critical response governing solute dispersion is observed over a wide range of oscillatory Reynolds numbers, which provides a novel control paradigm for microfluidic mixing and separation. Additionally, through a comparative analysis of fractional Maxwell, classical Maxwell and Newtonian fluids, we show that microscopic structural relaxation plays a crucial role in macroscopic solute transport under multi-field coupling. Our findings help to reveal flow mechanisms for precise mass transport control in electromagnetically coupled systems, advancing the development of microfluidic devices and biomedical detection technologies.

Key words: dispersion, MHD and electrohydrodynamics, microscale transport

© The Author(s), 2026. Published by Cambridge University Press.

https://doi.org/10.1017/jfm.2026.12134 Published online by Cambridge University Press

1. Introduction

Axial solute dispersion in micro/nano-fluidic systems holds significant theoretical importance and practical applications, with its regulation directly influencing the efficiency of critical processes such as micro-mixing (Dong *et al.* 2014; Liao *et al.* 2015), separation analysis (Ghosal & Chen 2012; Dhellemmes *et al.* 2024) and electrophoresis (Ghosal 2006). Over recent decades, alongside the rapid advancement of microfluidic technology, this field has demonstrated broad application prospects in scenarios such as biomedicine, chemical synthesis and point-of-care diagnostics. Meanwhile, active control strategies for axial dispersion have continuously evolved, including: modulating flow characteristics via applied pressure gradients (Rana & Murthy 2016*a*; Azari & Sadeghi 2022); regulating solute diffusion behaviour using electric fields (Rubinstein & Zaltzman 2013); introducing magnetic fields to induce Lorentz forces and alter solute diffusions (Vargas *et al.* 2017); engineering interfacial interactions through surface modification techniques (Sadeghi *et al.* 2020).

In microfluidic systems, electro-osmosis (EO) attracts significant research interest due to its unique capability for pump-free fluid propulsion. Introducing magnetic fields to establish an additional magnetohydrodynamic (MHD) effect creates a novel fluid manipulation mechanism, enabling fine-scale regulation of hydrodynamic characteristics through the interaction between electromagnetic fields and fluids. Additionally, the synergistic combination of hydrophobic wall slip characteristics and slip-dependent zeta potential further enhances fluid behaviour control. Therefore, this study investigates how interface slip and slip-dependent zeta potential modulate solute dispersion in viscoelastic solutions under oscillatory electro-osmotic flow (EOF) coupled with MHD, developing enhanced technology for precise control of microscale mass transport.

1.1. *Theoretical models for solute dispersion*

Theoretical research on dispersion models has long attracted the attention of researchers. Taylor's pioneering work (Taylor 1953) laid the foundation for solute dispersion modelling in pressure-driven pipe flows. This model relies on transverse concentration averaging, which requires an initial phase for radial diffusion to homogenise cross-sectional concentration profiles. This process is characterised by the dimensionless time scale $D_m t/R^2$ (where t, D_m and R denote time, molecular diffusivity and pipe radius, respectively), restricting the model's validity to long-time regimes. To overcome these limitations, Aris extended Taylor's dispersion theory using the moment method for an infinitely long pipe (Aris 1956). He derived a second-moment equation to describe the average concentration distribution under steady advection and demonstrated that, over sufficiently long times, solute tracers evolve into a Gaussian distribution due to the mean flow field. This research further refined the applicability and descriptive capability of Taylor dispersion theory. Subsequently, the methodologies based on the models proposed by Taylor and Aris were improved by Chatwin (1970), Barton (1983), Jimenez & Sullivan (1984), Mazumder & Das (1992) and Wu & Chen (2014).

Over the years, numerous studies have examined solute transport behaviour under different conditions, such as porous layers (Dentz *et al.* 2018; Das *et al.* 2024*a*), MHD flows (Vargas *et al.* 2017; Poddar *et al.* 2024; Das *et al.* 2024*b*; Sen *et al.* 2025), pollutant emissions in floating wetlands (Ai *et al.* 2022), by improving Taylor's model. However, these studies have only analysed solute diffusion at long times after injection into the fluid and have not provided any information on solute diffusion during the short time

https://doi.org/10.1017/jfm.2026.12134 Published online by Cambridge University Press

immediately following injection. Notably, Samuel *et al.* (2025) recently extended the Taylor dispersion in coupled electro-osmotic and pressure-driven flows across all time regimes under the assumptions of a low zeta potential, the Debye-Hückel approximation and a finite electric double layer (EDL) thickness. Initial studies sought to characterise band broadening dynamics immediately following injection, Gill & Sankarasubramanian (1970) put forth a general model, which articulates the transport coefficients as functions of time within steady-state flow. Subsequently, a series of advancements have been made. These include the consideration of a time-variable flow (Gill & Sankarasubramanian 1972; Sankarasubramanian & Gill 1972; Vedel & Bruus 2012), oscillating flow (Rana & Murthy 2016*a*; Azari & Sadeghi 2022), the non-uniformity of the injected solute band (Gill & Sankarasubramanian 1971, 1972) and interfacial/boundary mass transfer processes (Sankarasubramanian & Gill 1973; Rana & Murthy 2016*a*). In the present study, we are set to carry out a comprehensive exploration of the solute dispersion driven by the combined effects of MHD and oscillating EOF. Our research builds upon the generalised dispersion model that was introduced by Gill & Sankarasubramanian (1970).

1.2. *Solute dispersion in microchannels driven by EOF and MHD*

The manipulation of fluid flow and dispersion in microchannels via EOF represents a foundational area of inquiry in microfluidics owing to its attributes of operational simplicity, high controllability, uniform flow velocity profiles and reliance on non-mechanical actuation (Sadr *et al.* 2004; Goyal *et al.* 2024; Mehta & Mondal 2024). For nearly a century, the literature has systematically investigated various aspects of hydrodynamic dispersion in direct-current (DC) EO. Huang *et al.* (2024) showed that in transient Taylor–Gill dispersion during EOF, the peak concentration attenuates with increasing reaction intensity. Through multiscale analysis, Subudhi *et al.* (2024) found that stronger coupling parameters significantly slow solute transport in micropolar EOF within rectangular microchannels. Ponalagusamy & Murugan (2023) revealed that the EDL effect enhances solute diffusion in Carreau fluid under combined pressure-driven flow and EOF. Schulz *et al.* (2024) developed a novel effective dispersion model accounting for Taylor–Aris dispersion, EO-induced dispersion and their coupling. They theoretically proved the positivity of the dispersion coefficient and the existence and uniqueness of strong solutions, and numerically demonstrated the feasibility of charged species separation. Additionally, researchers have persistently pursued inquiries in this domain to examine the impacts of diverse supplementary facets of electrokinetic phenomena on solute transport and mixing dynamics (Arcos *et al.* 2018; Mukherjee *et al.* 2020; Mozafari *et al.* 2025).

Beyond conventional DC-EOF systems, alternating-current (AC)-EOF governs dynamic dispersion through electric field and EDL interactions to optimise dispersion and mixing processes in microfluidic systems. Li & Jian (2017) presented a focused investigation into solute dispersion induced by AC-EOF of viscoelastic fluids, with series expansion and transform techniques employed for analysis. Reshadi & Saidi (2019) found that in oscillatory EO-Poiseuille flow through polyelectrolyte-grafted capillaries, the polyelectrolyte layer (PEL) enhances solute advection and dispersion. A thicker charged PEL strengthens electro-osmotic advection, flattening transverse concentration and increasing radial differences. Mederos *et al.* (2020) theoretically investigated mass transfer in a microcapillary connecting two reservoirs with different concentrations of an electro-neutral solute. Results show that fluid elasticity–oscillatory flow interplay can enhance mass transfer rates by orders of magnitude compared with Newtonian oscillatory EOF. Peralta *et al.* (2020) investigated the mass transfer of Maxwell fluids in concentric annular microchannels driven by an AC-EOF. The analysis demonstrates that

https://doi.org/10.1017/jfm.2026.12134 Published online by Cambridge University Press

optimising the elasticity number, cylindrical gap and angular Reynolds number rationally can augment the total mass transfer rate and facilitate component separation. Subsequently, extensive research on solute transport driven by AC-EOF has primarily focused on the following key directions: dispersion analysis in microchannels with diverse geometries (Vargas *et al.* 2023), solute dispersion in nanochannels enclosed by a dielectric liquid layer (Chowdhury *et al.* 2025), the coupling effects of non-uniform walls (Dehe *et al.* 2021), regulatory mechanisms of asymmetric wall zeta potentials and slip interfaces (Huang *et al.* 2022), as well as the regulatory mechanisms of high zeta potentials and slip interfaces (Saha & Kundu 2022) on solute transport properties. In this work, an AC electric field is employed due to its superior performance in solute dispersion and microfluidic control. Its periodic polarity reversal suppresses electrode polarisation and electrolysis, thereby avoiding the unstable EOF and band broadening associated with DC fields. The oscillating field drives solutes into reciprocating motion, enhancing mixing and dispersion efficiency. Electrokinetic effects can be flexibly tuned by adjusting the frequency and amplitude, while high-frequency operation reduces Joule heating and improves system stability. These merits make AC electric fields highly suitable for microfluidic and biological applications.

In recent years, electric fields, magnetic fields and their synergy are widely used to precisely control microfluidic flows, with broad prospects in chemical and biomedical engineering involving mass and heat transport. In the study of EO and MHD flows, Joule heating and viscous dissipation constitute key thermal and mechanical effects. Chakraborty *et al.* (2013) reported that under constant wall heat flux, both effects reduce the Nusselt number via distinct mechanisms: Joule heating uniformly elevates bulk fluid temperature and weakens the wall temperature gradient, while viscous dissipation intensifies near the wall and raises wall temperature, both deteriorating heat transfer. Xie & Jian (2017) quantified entropy generation in two-layer MHD and EOF with Joule heating, finding that the entropy generation rate decays from the wall to interface and is dominated by the Hartmann number and viscous dissipation. Yang *et al.* (2019) investigated MHD-EOF and heat transfer in rectangular microchannels, demonstrating that heat transfer is jointly affected by Joule heating, viscous dissipation and electromagnetic coupling, where increased viscous dissipation impairs heat transfer while a larger electrokinetic width promotes it. Rilwan *et al.* (2024) further examined the influences of Joule heating and viscous dissipation on electromagnetohydrodynamic flow and heat transfer in porous microchannels. Furthermore, the coupled driving of MHD and EOF enables precise regulation of solute dispersion paths, thereby offering a new paradigm for the multi-field synergistic control of microscale mass transfer processes. Poddar *et al.* (2024) showed that strong magnetic fields significantly reduce flow velocity and the Taylor dispersion coefficient in two-dimensional MHD Taylor dispersion through parallel channels. Vargas *et al.* (2017) and Das *et al.* (2024*b*) applied Aris' method of moments to Newtonian solute dispersion in EO-MHD flows through parallel plate microchannels. Specifically, Vargas *et al.* (2017) found that slow sinusoidal wall zeta potential variations, combined with EO-MHD forces, significantly alter the axial distribution of the effective dispersion coefficient. Das *et al.* (2024*b*) explored the regulatory effects of symmetric and asymmetric zeta potentials on solute distribution, demonstrating that asymmetric zeta potentials accelerate the dispersion process. Subsequently, Sen *et al.* (2025) introduced heterogeneous first-order boundary reactions and transverse electric fields to further investigate the solute dispersion characteristics of non-Newtonian fluids under the combined effects of MHD and EOF in parallel plate microchannels. All their core conclusions are fundamentally based on Aris' method. Notably, Joule heating has been consistently neglected in existing studies on solute dispersion in MHD and EOF-driven flows. This indicates that while Joule heating is indispensable in heat transfer-focused analyses of MHD and EOF systems,

https://doi.org/10.1017/jfm.2026.12134 Published online by Cambridge University Press

neglecting it in studies concentrating on solute dispersion is a common and reasonable practice. This simplification is not an oversight, but rather reflects the physical consensus in the field that thermal effects are always secondary to the hydrodynamic mechanisms of interest in such problems. In line with this established research paradigm, the present study focuses on elucidating the fundamental regulatory mechanism of electromagnetic forces on solute dispersion over a wide range of magnetic field intensities. Within the parameter range explored, the temperature rise induced by Joule heating is negligible, and it is therefore justifiably excluded from the analysis.

1.3. *Microchannel interfacial slip and slip-dependent zeta potential*

In microscale fluid mechanics, the extremely small characteristic scales (at the micrometre level) and high surface-area-to-volume ratios make surface properties a core determinant of flow behaviour. Notably distinct from macroscopic flows, hydrodynamic slip at microscale liquid–solid interfaces is a prevalent phenomenon, whereby traditional no-slip models often require modification due to their inadequacy (Thompson & Troian 1997; Zhu & Granick 2001, 2002). This attribute is critical in microscale EOF. First, interfacial slip directly alters the flow field. In hydrophobic microchannels, non-wetting conditions exacerbate the breakdown of the no-slip assumption, making slip length an essential parameter (Hegde & Harikrishnan 2021; Sujith *et al.* 2025). Second, wall slip modifies the relationship between surface potential and zeta potential. Specifically, slip leads to an apparent increase in zeta potential, which manifests as a reduced velocity gradient within the EDL (Joly *et al.* 2006).

The interplay between interfacial slip and zeta potential has been a focal point of research in recent decades. Owing to the strong coupling between these two factors, the independent measurement of electrokinetic phenomena on hydrophobic surfaces remains challenging. Early investigations by Churaev *et al.* (2002) established a linear relationship model between slip length and zeta potential through experiments on methylated quartz capillaries. Subsequent studies by Yang & Kwok (2002) and Tandon & Kirby (2008) further refined this theoretical framework. This mechanistic understanding highlights that traditional surface potential models based on the no-slip assumption are no longer capable of accurately describing microscale transport characteristics, with the interaction between interfacial slip and electrochemical properties emerging as a critical factor in explaining physical processes within microfluidic devices.

Recently, research on surface slip and slip-dependent zeta potential has made significant progress in the field of microscale fluid dynamics, spanning fluid flow, heat transfer mechanisms, energy conversion systems and solute dispersion processes in EOF, MHD flow and EO-MHD coupled flow. Banerjee *et al.* (2021) showed that traditional surface potential models (neglecting slip) underestimate core flow velocity in combined electro-osmotic pressure-driven microchannels. Banerjee *et al.* (2023) found that slip-induced zeta potential increase strengthens EO force and enhances near-wall velocity in pulsatile EO and shear-driven flows. Siva *et al.* (2024) confirmed that slip-dependent zeta potential governs rotational flow and volume transport in EO-MHD couple stress flows in rotating microchannels. Deng *et al.* (2024) demonstrated that slip-dependent zeta potential significantly enhances the sensitivity of two-layer flow parameters in unsteady cylindrical EOF. Other recent studies on the EO and MHD transport of viscoelastic fluids in microchannels with slip-dependent zeta potential have revealed several critical advances. The slip-dependent zeta potential significantly optimises the electrokinetic energy conversion process (Saha & Kundu 2023; Liu *et al.* 2024; Saha & Kundu 2025); strengthening the coupling between interfacial charges and fluid slip remarkably

https://doi.org/10.1017/jfm.2026.12134 Published online by Cambridge University Press

modifies the electromagnetic transport properties (Das *et al.* 2025) and thermal entropy characteristics (Siva *et al.* 2023) in a microchannel.

Notably, the influence of interfacial slip on solute dispersion has sparked extensive discussion (Li & Jian 2019; Huang *et al.* 2022; Saha & Kundu 2022). The investigation of coupled slip-dependent zeta potential and viscoelastic effects of Carreau fluids in two-fluid EOF demonstrated that slip modifies diffusion kinetics by enhancing the apparent zeta potential, with shear-thinning/thickening behaviour further amplifying this effect (Kuntal *et al.* 2025). However, the solute dispersion characteristics in the combined driving regime of AC-EOF and MHD with slip-dependent zeta potential remain unexplored in existing literature.

1.4. *The position and structure of the current work*

Based on a comprehensive review of recent advancements in solute dispersion studies within microfluidic systems, it has been found that EOF and the hybrid EO-MHD approach for fluid flow and mass transport have emerged as a prominent frontier in multi-physics microscale transport research. This synergistic strategy integrates the high driving efficiency of EO with the superior dispersion-suppression capability of MHD, enabling better controllability than single actuation modes. It exhibits great potential for applications including biochemical separation, targeted drug delivery and microfluidic reaction systems (Sahore *et al.* 2018; Chaudhuri *et al.* 2018; Zhang *et al.* 2025), where stable transport and tuneable dispersion are essential. Nevertheless, current research still suffers from several limitations, as detailed below.

First, a key challenge in this field is that, whereas research has predominantly focused on Newtonian fluids (Reshadi & Saidi 2019; Sadeghi *et al.* 2020; Das *et al.* 2024*b*; Samuel *et al.* 2025) and select non-Newtonian fluids (Sen *et al.* 2025) within microchannels, the governing mechanisms of coupled magneto-electrodynamic fields on solute dispersion in viscoelastic fluids remain elusive. Given the prevalence of such fluids in industrial applications of axial dispersion, elucidating their behaviour is critical. This lack of mechanistic insight across broad parameter spaces hinders the development of general principles for dispersion.

Second, current research on the influence of microscale interfacial characteristics on solute dispersion processes remains insufficient. Most existing studies are based on the no-slip assumption (Reshadi & Saidi 2019; Sadeghi *et al.* 2020; Das *et al.* 2024*b*; Samuel *et al.* 2025; Sen *et al.* 2025), which exhibits significant limitations in microscale flows. Moreover, the majority of related work has focused only on the role of single factors, such as heterogeneous or asymmetric zeta potentials at the wall (Vargas *et al.* 2017; Das *et al.* 2024*b*), without incorporating the combined effects of interfacial slip and zeta potentials.

Third, although Gill's generalised dispersion model shows higher reliability in describing the transient processes of solute dispersion, its inherent complexity in mathematical derivation has resulted in limited adoption in practical microfluidic systems.

Against this backdrop, building on an extension of Gill's generalised dispersion model, this study seeks to (i) systematically investigate the solute dispersion behaviour in polymer solutions within microchannels under the drive of MHD-AC-EOF multiphysics coupling, and (ii) further elucidate the regulatory role of microscale interfacial effects, specifically interfacial slip characteristics and slip-dependent zeta potential, in this dispersion process. The findings will offer more comprehensive theoretical underpinnings for optimising the separation and mixing performance of microfluidic devices.

The remainder of this paper is structured as follows. The subsequent section first systematically describes the flow geometry configuration and explicitly outlines the

https://doi.org/10.1017/jfm.2026.12134 Published online by Cambridge University Press

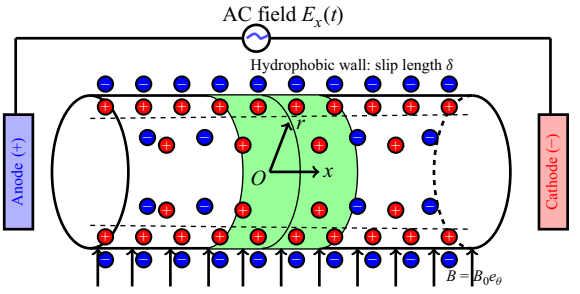


Figure 1. The diagram of the MHD-AC-EOF in a microtube with a slip-dependent zeta potential.

physical problem formulation along with key assumptions. Section 3 outlines the governing equations for MHD-AC-EOF and solute dispersion in polymer solutions; specifically, the development of models for several types of complex polymer solutions and the estimation of their corresponding parameters are detailed in Appendix A; additionally, the corresponding analytical solution algorithms are proposed. Section 4 presents the core results of this study, including the validation of the proposed model and corresponding simulation results, alongside an in-depth mechanism analysis underlying the effects of major dimensionless parameters on solute dispersion behaviour under both AC-EOF and mixed MHD-AC-EOF regimes. Finally, § 5 concludes the paper with discussions on the results.

2. Problem description and assumptions

As shown in figure 1, the unsteady flow characteristics and dispersion phenomena in viscoelastic solutions (such as polymer solutions) through a microtube under the coordinated driving of an AC electric field and a magnetic field are considered. A cylindrical coordinate system is adopted, with its origin precisely situated at the centre of the tube. In this coordinate system, r represents the radial distance measured from the central axis of the tube, while x denotes the axial coordinate. The microtube has a radius R and is sufficiently long such that the flow is fully developed and all physical quantities are independent of the axial coordinate x. The dispersion process commences at $t = 0$ with the instantaneous injection of a minute quantity of solute. This solute is uniformly distributed across the cross-section at $x = 0$ and subsequently propelled by the MHD-AC-EOF within the flexible microtube. It is postulated that the injected solute band is sufficiently dilute such that the flow of the carrier fluid remains unaffected by the presence of trace-level soluble substances. In this study, the research objectives are pursued in a sequential manner. Initially, an analysis of the dynamic behaviours of MHD-AC-EOF is performed, which holds significant importance for studies on solute dispersion driven by MHD-AC-EOF. After that, the dispersion characteristics of the solutes injected into the tube will be analysed under two distinct scenarios: pure AC-EOF and mixed MHD-AC-EOF. The following sections elaborate on these aspects in detail.

3. Mathematical analysis of electric potential, velocity and concentration fields

Currently, we are preparing to conduct an analysis of MHD-AC-EOF and solute dispersion in a narrow tube with a slip-dependent zeta potential. The velocity for the MHD-AC-EOF and concentration for solute dispersion are determined by momentum conservation and mass transport. In the case of considering a symmetric electrolyte solution, the continuity

https://doi.org/10.1017/jfm.2026.12134 Published online by Cambridge University Press

equation, Navier–Stokes equation and the convective diffusion equation can be given in the following forms:

$$\bar{\boldsymbol{\nabla}} \cdot \bar{\boldsymbol{V}} = 0, \tag{3.1}$$

$$\rho \frac{\partial \bar{\boldsymbol{V}}}{\partial t} + \rho \left(\bar{\boldsymbol{V}} \cdot \bar{\boldsymbol{\nabla}} \bar{\boldsymbol{V}} \right) = \boldsymbol{\nabla} \cdot \bar{\boldsymbol{T}} + \bar{\boldsymbol{F}}, \tag{3.2}$$

$$\frac{\partial \bar{C}}{\partial t} + \bar{\boldsymbol{\nabla}} \cdot \left(\bar{\boldsymbol{V}} \bar{C} \right) = D \bar{\boldsymbol{\nabla}} \cdot (\bar{\boldsymbol{\nabla}} \bar{C}). \tag{3.3}$$

In (3.1)–(3.3), $\bar{\boldsymbol{V}}$ and $\bar{\boldsymbol{T}}$ are the velocity vector and stress tensor, respectively, ρ is fluid density, t is time, and $\bar{C}$ and D are the concentration field and molecular diffusivity, respectively. Moreover, $\bar{\boldsymbol{F}}$ represents the body force acting on the fluid, originating from the electromagnetic interactions imposed on the system and potentially contributed by

$$\bar{\boldsymbol{F}} = \bar{\rho}_e \bar{\boldsymbol{E}} + \bar{\boldsymbol{J}} \times \bar{\boldsymbol{B}}. \tag{3.4}$$

In this formulation, $\bar{\rho}_e = e \sum_l z_l n_l$ is the charge density, in which e is the basic electric charge, n_l and z_l are the molar concentration and charge valence of space l, respectively, $\bar{\boldsymbol{E}}$ is the applied electric field with a strength of $E_x(t)$ in the x direction and $\bar{\boldsymbol{B}}$ represents the applied magnetic field with magnitude B_0 in the θ direction, which is symmetrically distributed around the circumference of the microtube cross-section. At each circumferential position, the magnetic field vector is locally tangential, perpendicular to the plane formed by the central axis and the radial direction and acts uniformly on all fluid elements across the entire cross-section. Here $\bar{\boldsymbol{J}}$ signifies the local ion current density defined by Ohm's law,

$$\bar{\boldsymbol{J}} = \sigma_e (\bar{\boldsymbol{E}} + \bar{\boldsymbol{V}} \times \bar{\boldsymbol{B}}), \tag{3.5}$$

where σ_e is the electrical conductivity.

3.1. *Electric potential distribution with slip dependent zeta potential*

We first evaluate the magnetic Reynolds number Re_m to assess the validity of neglecting the induced magnetic field. For MHD flow in the microtube, the magnetic Reynolds number is defined as $Re_m = U_m L / \eta_m$, where U_m is the characteristic velocity, L is the characteristic length and $\eta_m = 1/(\mu \sigma_e)$ is the magnetic diffusivity, with σ_e the electrical conductivity of the fluid and μ the magnetic permeability. Using the typical parameter ranges given in § 4 (e.g. $L = 10$–250 μm, $\sigma_e = 2.2 \times 10^{-4}$–$10^6$ S m^{-1}, $U_m \approx 1$ m s^{-1} and $\mu = \mu_0 = 4\pi \times 10^{-7}$ H m^{-1}), the calculated magnetic Reynolds number ranges from approximately 2.8×10^{-15} to 3.1×10^{-4}, which is much less than unity. Under this condition, the induced magnetic field is negligible and the applied external magnetic field remains unaffected by the flow field. The potential $\bar{\Psi}$ in the channel can be considered as the electrostatic potential and is generated by the superposition of external potential $\bar{\varphi}$ and surface charge potential (EDL potential) $\bar{\psi}$ on the microchannel wall. Assuming that the microchannel is very long and any end effects are ignored, the EDL potential can be considered as independent of the axial position in the microchannel, and the total potential can be expressed

$$\bar{\Psi} = \bar{\varphi} + \bar{\psi}. \tag{3.6}$$

Following Gauss's law, the electric potential equation can be decomposed into two equations:

https://doi.org/10.1017/jfm.2026.12134 Published online by Cambridge University Press

$$\varepsilon \bar{\nabla}^2 \bar{\varphi} = 0, \tag{3.7}$$

$$\varepsilon \bar{\nabla}^2 \bar{\psi} = -\bar{\rho}_e. \tag{3.8}$$

Here ε is the permittivity of the fluid. According to the electrostatic theory of aqueous electrolyte solutions adjacent to charged surfaces, the ionic concentration n_l displays a spatial gradient extending from the capillary wall to its central axis. Under the assumption of equilibrium conditions for electrolyte solutions across the entire capillary cross-section, the ionic concentration conforms to a Boltzmann distribution, i.e.

$$n_l = n_l^{\infty} \exp\left(-\frac{e z_l \bar{\psi}}{k_b T}\right). \tag{3.9}$$

Here n_l^{∞} is defined as the bulk concentration of ion l under the neutral condition where the electric potential $\bar{\psi}$ equals zero. By combining (3.8) and (3.9), the Poisson–Boltzmann equation governing the electric potential distribution in the microchannel is mathematically derived as

$$\varepsilon \bar{\nabla}^2 \bar{\psi} = -e \sum_l z_l n_l^{\infty} \exp\left(-\frac{e z_l \bar{\psi}}{k_b T}\right). \tag{3.10}$$

This model provides a fundamental framework for describing ion transport phenomena in microfluidic systems (Wang & Kang 2010). Given the challenges associated with obtaining analytical solutions to the complete set of electrokinetic equations, three primary approximation frameworks have been established over the years. These methodologies are specifically tailored to scenarios characterised by thin EDLs, weak field/flow conditions and low surface electric potential, respectively. (i) If the thickness of the EDL (approximated by the Debye length λ_D) is significantly smaller than the system's characteristic length scale ($\lambda_D/L \ll 1$), specifically, fluid flow of a Newtonian electrolyte (Debye length $\lambda_D \sim \mathcal{O}(10^{-9}\text{m})$) in a microchannel with complex geometry ($L \sim \mathcal{O}(10^{-5}\text{m})$), and under the assumption of quasi-laminar flow within the EDL, then the EDL effect can be approximated by a surface slip velocity. This approach circumvents the need to resolve the flow field within the EDL. (ii) The Helmholtz–Smoluchowski theory, $\boldsymbol{u}_{HS} = \mu \boldsymbol{E}$, is canonically employed to model this slip velocity under such scenarios (Chen *et al.* 2023; Wang *et al.* 2023). Importantly, slip boundary conditions inherently fail to resolve microscale phenomena occurring within the EDL. (iii) The low-surface-potential assumption (i.e. $|e z_l \psi / k_b T| < 1$) can be adopted. This enables the application of the Debye–Hückel linearisation to (3.10) (Li 2004; Masliyah & Bhattacharjee 2006). In this paper, for symmetric electrolyte solutions ($z^+ = -z^- = z$, $D^+ = D^- = D$) confined within micro/nanotubular geometries under low-surface-potential conditions, the Poisson–Boltzmann equation can be expressed in cylindrical coordinates and linearised via the Debye–Hückel approximation as the following dimensionless form:

$$\frac{\partial^2 \psi}{\partial r^2} + \frac{1}{r}\frac{\partial \psi}{\partial r} = \kappa^2 \psi. \tag{3.11}$$

Here the subsequent collection of dimensionless quantities is utilised: $\psi = e z \bar{\psi}/k_b T$, $r = \bar{r}/R$ and $\kappa = R/\lambda_D$ is known as the Debye parameter, where $\lambda_D = (2 n^{\infty} e^2 z^2/\varepsilon k_b T)^{-1/2}$ is the Debye length.

The quantitative relationship between the surface zeta potential and the slip length was first derived by Churaev *et al.* (2002) as an analytical model, which can be expressed in

https://doi.org/10.1017/jfm.2026.12134 Published online by Cambridge University Press

the dimensionless form: $\zeta_\delta = \zeta(1+\delta\kappa)$. Here, $\zeta_\delta = \bar{\zeta}_\delta ez/k_bT$ and $\zeta = \bar{\zeta} ez/k_bT$ denote the dimensionless form of zeta potentials under slip and no-slip boundary conditions, respectively, with $\delta = \bar{\delta}/R$ defined as the dimensionless slip length parameter governing interfacial hydrodynamic effects. Subsequently, Yang & Kwok (2002) introduced a modification factor f_m to establish the adjusted zeta potential formulation $\zeta_\delta = \zeta(1+\delta\kappa)/f_m$. Most recently, Tandon & Kirby (2008) developed a nonlinear slip-dependent zeta potential model for a symmetric $z:z$ electrolyte expressed as

$$\zeta_\delta = \zeta\left(1+\delta\kappa\frac{\sinh\zeta}{\zeta}\right). \tag{3.12}$$

The core physical significance of this model is that it quantitatively reveals the strong coupling between solid–liquid interfacial slip and EDL electrokinetic properties in micro/nano-fluidic systems, providing a unified, precise theoretical framework for interpreting complex electrokinetic transport at hydrophobic interfaces. This analytical framework has been extensively adopted in contemporary investigations of electro-osmotic transport within microfluidic systems (Vasista *et al.* 2021, 2022; Banerjee *et al.* 2021, 2023; Siva *et al.* 2024; Deng *et al.* 2024). Particularly, we utilise this theoretical relationship to quantitatively determine the interfacial electric potential distribution along the microchannel surfaces. The suitable boundary conditions required to solve (3.11) are enumerated as follows:

$$\psi|_{r=0} = \text{finite}, \quad \left.\frac{\mathrm{d}\psi}{\mathrm{d}r}\right|_{r=0} = 0, \quad \psi|_{r=1} = \zeta_\delta. \tag{3.13}$$

Under the condition of slip-dependent zeta potential, the Debye–Hückel approximation is valid when $|\zeta_\delta| < 1$, and this condition can be guaranteed by imposing the constraint $\delta\kappa < (1-|\zeta|)/\sinh|\zeta|$ (with $|\zeta| < 1$ for the non-slip zeta potential). Consequently, by applying the stated boundary conditions, the dimensionless analytical solutions to (3.11) and the expression for charge density ρ_e are obtained as

$$\psi = \zeta\left(1+\delta\kappa\frac{\sinh\zeta}{\zeta}\right)\frac{I_0(\kappa r)}{I_0(\kappa)}, \quad \rho_e = \kappa^2\psi, \tag{3.14}$$

where $I_0(r)$ is the modified Bessel function of the first kind of order zero (Watson 1995). Analogously, with respect to the slip-independent zeta potential, the mathematical representation of ψ is given by

$$\psi = \zeta\frac{I_0(\kappa r)}{I_0(\kappa)}. \tag{3.15}$$

3.2. *Velocity distribution*

With the electric potential distribution within the microtube now determined, we can compute the electrokinetic body force for incorporation into the Navier–Stokes equation. This enables us to analytically solve for the transient velocity profile in the microtube. Given the axisymmetric geometry and the elongated, narrow configuration characteristic of microfluidic channels, the axial velocity component exhibits independence on θ and x. The velocity field therefore reduces to $\boldsymbol{V} = (0, 0, u(r,t))$ in cylindrical coordinates, inherently satisfying the continuity equation for this constrained flow. Through simplification of the viscoelastic constitutive relation (A5) for the rectilinear flow geometry and subsequent substitution into the momentum equation, governing equations

https://doi.org/10.1017/jfm.2026.12134 Published online by Cambridge University Press

for the velocity distribution can be reformulated as

$$\left(1+\lambda^{\alpha-\beta}\frac{\partial^{\alpha-\beta}}{\partial\bar{t}^{\alpha-\beta}}\right)\left(\rho\frac{\partial\bar{u}}{\partial\bar{t}}+\sigma_e B_0^2\bar{u}\right)$$
$$=\eta\lambda^{\alpha-1}\frac{\partial^{\alpha-1}}{\partial\bar{t}^{\alpha-1}}\frac{1}{\bar{r}}\frac{\partial}{\partial\bar{r}}\left(\bar{r}\frac{\partial\bar{u}}{\partial\bar{r}}\right)+\bar{\rho}_e(\bar{r})\left(1+\lambda^{\alpha-\beta}\frac{\partial^{\alpha-\beta}}{\partial\bar{t}^{\alpha-\beta}}\right)\bar{E}_x(\bar{t}). \tag{3.16}$$

As previously discussed, the applied electric field and resulting flow velocity each contain harmonic oscillating components with identical angular frequency (ω). Consequently, these quantities can be represented in complex form as

$$\left\langle\bar{u}(\bar{r},\bar{t}),\ \bar{E}_x(\bar{t})\right\rangle=\mathrm{Im}\ \left\{\left\langle\bar{u}_0(\bar{r}),\ \bar{E}_0\right\rangle\exp(\mathrm{i}\bar{\omega}\bar{t})\right\}. \tag{3.17}$$

In this mathematical formulation, $\mathrm{i}=\sqrt{-1}$ denotes the imaginary unit, while Im designates the imaginary component of a complex number. Substituting (3.17) into (3.16) and equating the coefficients of the exponential term in the resulting equation on both sides, the following expression can be derived:

$$\eta\lambda^{\alpha-1}(\mathrm{i}\bar{\omega})^{\alpha-1}\left(\frac{\mathrm{d}^2\bar{u}_0(\bar{r})}{\mathrm{d}\bar{r}^2}+\frac{1}{\bar{r}}\frac{\mathrm{d}\bar{u}_0(\bar{r})}{\mathrm{d}\bar{r}}\right)$$
$$-\left[1+\lambda^{\alpha-\beta}(\mathrm{i}\bar{\omega})^{\alpha-\beta}\right]\left(\rho\mathrm{i}\bar{\omega}\bar{u}_0(\bar{r})+\sigma_e B_0^2\bar{u}_0(\bar{r})\right)=-\bar{\rho}_e(r)\left[1+\lambda^{\alpha-\beta}(\mathrm{i}\bar{\omega})^{\alpha-\beta}\right]. \tag{3.18}$$

For analytical tractability, substituting the charge density expression via (3.14) and performing proper scaling, (3.18) can be further cast into the following dimensionless form:

$$\frac{\mathrm{d}^2u_0(r)}{\mathrm{d}r^2}+\frac{1}{r}\frac{\mathrm{d}u_0(r)}{\mathrm{d}r}-\left(\mathrm{i}^{1-\alpha}De^{1-\alpha}+\mathrm{i}^{1-\beta}De^{1-\beta}\right)(Re\mathrm{i}+Ha^2)u_0(r)$$
$$=-\kappa^2\zeta\left(\mathrm{i}^{1-\alpha}De^{1-\alpha}+\mathrm{i}^{1-\beta}De^{1-\beta}\right)\left(1+\kappa\delta\frac{\sinh\zeta}{\zeta}\right)\frac{I_0(\kappa r)}{I_0(\kappa)}. \tag{3.19}$$

Within the preceding equation, the dimensionless variables are hereinafter denoted as $r=\bar{r}/R$, $\psi=\bar{\psi}ez/k_bT$, $\kappa=\bar{\kappa}R$, $u=\bar{u}/U_{EO}$, $\omega=\bar{\omega}/\omega_{ref}$, $t=\bar{t}\omega_{ref}$, $De=\lambda\bar{\omega}$, $Re=\rho\bar{\omega}R^2/\eta$, $Ha=B_0R\sqrt{(\sigma_e/\eta)}$, where $U_{EO}=-\varepsilon k_bTE_0/\eta ze$ represents the Helmholtz–Smoluchowski velocity, $\omega_{ref}=D/R^2$ is the reference frequency and De, Re and Ha denote the Deborah number, oscillation Reynolds number and Hartmann number, respectively. To solve (3.19), the following conditions are defined: the value of velocity should be finite at the centre of the capillary, velocity needs to meet the axial-symmetry requirement, a slip condition holds at the capillary wall. Each of these conditions can be expressed in the following dimensionless forms, respectively:

$$\left.\begin{aligned}&u_0(r)|_{r=0}=\text{finite},\quad \left.\frac{\mathrm{d}u_0(r)}{\mathrm{d}t}\right|_{r=0}=0,\\&\left[u_0(r)+\delta\ \frac{\mathrm{d}u_0(r)}{\mathrm{d}r}\right]\Bigg|_{r=1}=0.\end{aligned}\right\} \tag{3.20}$$

https://doi.org/10.1017/jfm.2026.12134 Published online by Cambridge University Press

The solution of (3.19) and (3.20) can be derived as

$$u_0(r) = C_1\Big[C_2\mathrm{J}_0\big(i\sqrt{A}r\big) + C_3 r\mathrm{I}_0(\kappa r)\mathrm{I}_1\big(\sqrt{A}r\big)\mathrm{Y}_0\big(-\mathrm{i}\sqrt{A}r\big) - \mathrm{i}C_3 r\mathrm{I}_0(\kappa r)\mathrm{J}_0\big(i\sqrt{A}r\big)\mathrm{Y}_1\big(-i\sqrt{A}r\big) + C_4 r\mathrm{I}_1(\kappa r)\mathrm{J}_0\big(i\sqrt{A}r\big)\mathrm{Y}_0\big(-i\sqrt{A}r\big) - C_4 r\mathrm{I}_0\big(\sqrt{A}r\big)\mathrm{I}_1(\kappa r)\mathrm{Y}_0\big(-i\sqrt{A}r\big)\Big]. \quad (3.21)$$

The explicit expressions for coefficients $C_1 - C_4$ and the coupled parameter A are provided in Appendix B. Since the analytical velocity solution is mathematically involved, we performed an equivalent mathematical transformation to obtain a more compact form to facilitate the subsequent derivation and evaluation of the concentration distribution, with detailed derivations presented in Appendix B.

3.3. *Analysis of solute dispersion*

The generalised dispersion model developed by Gill & Sankarasubramanian (1970) employs time-varying dispersion coefficients to ensure applicability at all times after solute injection and is readily solvable for fully developed steady tube flow. In contrast, this study deals with a multi-field driven oscillatory flow with a complex velocity distribution. Due to this complexity, quantities such as $K_2(t)$ and $g_1(r, t)$ are solved using a method different from the reference (see (3.36)–(3.38) and Appendix C). The model is expressed in cylindrical coordinates as

$$\frac{\partial \bar{C}}{\partial \bar{t}} + \bar{u}(\bar{r}, \bar{t})\frac{\partial \bar{C}}{\partial \bar{x}} = D\left[\frac{\partial^2 \bar{C}}{\partial \bar{x}^2} + \frac{1}{\bar{r}}\frac{\partial}{\partial \bar{r}}\left(\bar{r}\frac{\partial \bar{C}}{\partial \bar{r}}\right)\right], \quad (3.22)$$

where $\bar{u}(\bar{r}, \bar{t})$ is the velocity of the MHD-AC-EOF. We assume that the injected solute is introduced at the initial time $\bar{t} = 0$ within a bandwidth of $\bar{x_s}$, and its concentration is set to $\bar{C_0}$. The concentration approaches zero as the spatial position extends to infinity. No mass transfer occurs at the wall surface and the concentration distribution exhibits perfect symmetry about the central axis. Then, the associated conditions can be rewritten as

$$\bar{C}(\bar{x}, \bar{r}, 0) = \bar{C}_0, \left(|\bar{x}| \le \frac{1}{2}\bar{x}_s\right), \quad \bar{C}(\bar{x}, \bar{r}, 0) = 0, \left(|\bar{x}| > \frac{1}{2}\bar{x}_s\right), \quad (3.23a)$$

$$\bar{C}(\infty, \bar{r}, \bar{t}) = 0, \quad \frac{\partial \bar{C}}{\partial \bar{r}}(\bar{x}, 0, \bar{t}) = \frac{\partial \bar{C}}{\partial \bar{r}}(\bar{x}, R, \bar{t}) = 0. \quad (3.23b)$$

The subsequent dimensionless variables are introduced for further analysis

$$C = \frac{\bar{C}}{\bar{C}_0}, \ \bar{x} = \frac{D\bar{x}}{R^2 U_{EO}}, \quad \bar{x}_s = \frac{D\bar{x}_s}{R^2 U_{EO}}, \quad r = \frac{\bar{r}}{R}, \quad t = \frac{D\bar{t}}{R^2}, \quad Pe = \frac{RU_{EO}}{D}. \quad (3.24)$$

Then, the aforesaid equation is capable of being expressed in the following dimensionless form:

$$\frac{\partial C}{\partial t} + u(r, t)\frac{\partial C}{\partial x} = \frac{1}{Pe^2}\frac{\partial^2 C}{\partial x^2} + \frac{1}{r}\frac{\partial}{\partial r}\left(r\frac{\partial C}{\partial r}\right), \quad (3.25a)$$

$$C(x, r, 0) = 1, \left(|x| \le \frac{1}{2}x_s\right), \quad C(x, r, 0) = 0, \left(|x| > \frac{1}{2}x_s\right), \quad (3.25b)$$

$$C(\infty, r, t) = 0, \quad \frac{\partial C}{\partial r}(x, 0, t) = \frac{\partial C}{\partial r}(x, 1, t) = 0. \quad (3.25c)$$

Here Pe is the Peclet number.

https://doi.org/10.1017/jfm.2026.12134 Published online by Cambridge University Press

For analysing the solute dispersion process, a new coordinate system is set up, in which the x axis moves a distance determined by calculating the mean velocity of the flow, i.e.

$$x_1 = x - \int_0^t U(t)\mathrm{d}t, \quad \text{where} \quad U(t) = 2\int_0^1 ru\mathrm{d}r = \mathrm{Im}\{U_1 \mathrm{e}^{\mathrm{i}\omega t}\}, \tag{3.26}$$

where $U(t)$ denotes the instantaneous cross-sectionally averaged velocity (with the radius normalised to unity) and $U_1 = 2\int_0^1 ru_0\mathrm{d}r$ represents its complex amplitude. Given the new coordinate system, (3.25*a*) can be reformulated as

$$\frac{\partial C}{\partial t} + (u-U)\frac{\partial C}{\partial x_1} = \frac{1}{Pe^2}\frac{\partial^2 C}{\partial x_1^2} + \frac{1}{r}\frac{\partial}{\partial r}\left(r\frac{\partial C}{\partial r}\right). \tag{3.27}$$

Adopting the method proposed by Gill & Sankarasubramanian (1970), the local concentration C is currently defined by a series expansion based on axis gradients of different orders of the area-average concentration C_m, i.e.

$$C = \sum_{p=0}^{\infty} g_p(r,t)\frac{\partial^p C_m}{\partial x_1^p}, \tag{3.28}$$

where

$$C_m = 2\int_0^1 rC\mathrm{d}r, \tag{3.29}$$

the function $g_p(r,t)$ bears resemblance to the Taylor expansion coefficient. By default, $g_0 = 1$. After substituting (3.28) into (3.27) , we obtain

$$\begin{aligned}&\frac{\partial C_m}{\partial t} + (u-U)\frac{\partial C_m}{\partial x_1} - \frac{1}{Pe^2}\frac{\partial^2 C_m}{\partial x_1^2} + \sum_{p=1}^{\infty}\left\{\left[\frac{\partial g_p}{\partial t} - \frac{1}{r}\frac{\partial}{\partial r}\left(r\frac{\partial g_p}{\partial r}\right)\right]\frac{\partial^p C_m}{\partial x_1^p}\right. \\ &\left.+(u-U)g_p\frac{\partial^{p+1} C_m}{\partial x_1^{p+1}} - \frac{1}{Pe^2}g_p\frac{\partial^{p+2} C_m}{\partial x_1^{p+2}} + g_p\frac{\partial^{p+1} C_m}{\partial t\partial x_1^p}\right\} = 0.\end{aligned} \tag{3.30}$$

Assuming the evolution of C_m is diffusive from time zero, we can formulate the generalised dispersion model in dimensionless form with time-dependent dispersion coefficients as

$$\frac{\partial C_m}{\partial t} = \sum_{j=0}^{\infty} K_j(t)\frac{\partial^j C_m}{\partial x_1^j}. \tag{3.31}$$

The coefficients $K_0(t)$, $K_1(t)$ and $K_2(t)$ denote the exchange, convection and dispersion coefficients, respectively, while $K_3(t)$ and $K_4(t)$ in (3.31) characterise the skewness and kurtosis of the solute concentration distribution during the dispersion process. Since the terms involving $K_0 - K_2$ are several orders of magnitude larger than the higher-order terms, the cross-sectional mean concentration profile can be accurately approximated using only the first three terms (Gill & Sankarasubramanian 1970). This convention is widely adopted in the relevant literature (Rana & Murthy 2016*a*; Reshadi & Saidi 2019; Sadeghi *et al.* 2020). In the present study, because the wall is impermeable and there is no mass exchange at the boundary, we have $K_0(t) = 0$. The coefficients $K_1(t)$ and $K_2(t)$ are determined next. Upon the substitution of (3.31) into (3.30), followed by the rearrangement

https://doi.org/10.1017/jfm.2026.12134 Published online by Cambridge University Press

of terms and taking into account the condition

$$\frac{\partial^{p+1} C_m}{\partial t \partial x_1^p} = \sum_{j=1}^{\infty} K_j(t) \frac{\partial^{j+p} C_m}{\partial x_1^{j+p}}, \tag{3.32}$$

an infinite set of differential equations is generated by equating the coefficients of $\partial^p C_m / \partial x_1^p$ to zero:

$$\frac{\partial g_1}{\partial t} = \frac{1}{r}\frac{\partial}{\partial r}\left(r\frac{\partial g_1}{\partial r}\right) - (u - U + K_1(t)), \tag{3.33a}$$

$$\frac{\partial g_2}{\partial t} = \frac{1}{r}\frac{\partial}{\partial r}\left(r\frac{\partial g_2}{\partial r}\right) - (u - U + K_1(t))\, g_1 - \left(K_2(t) - \frac{1}{Pe^2}\right), \tag{3.33b}$$

$$\begin{aligned}\frac{\partial g_{p+2}}{\partial t} = &\frac{1}{r}\frac{\partial}{\partial r}\left(r\frac{\partial g_{p+2}}{\partial r}\right) - (u - U + K_1(t))\, g_{p+1} \\ &- \left(K_2(t) - \frac{1}{Pe^2}\right) g_p - \sum_{j=3}^{p+2} K_j(t) g_{p+2-j}, \quad p = 1, 2, 3, \cdots.\end{aligned} \tag{3.33c}$$

Equations (3.31) and (3.33) formulate the transient dispersion problem associated with time-varying flow. In view of the initial and boundary conditions for C as presented in (3.25), and the definition of C_m in (3.29), the corresponding conditions for g_p can be derived as

$$g_p(0,\ r) = 0, \tag{3.34a}$$

$$\frac{\partial g_p}{\partial r}(t,\ 0) = \frac{\partial g_p}{\partial r}(t,\ 1) = 0, \tag{3.34b}$$

$$\int_0^1 r g_p \mathrm{d}r = 0. \tag{3.34c}$$

Multiplying (3.33a) by r and subsequently integrating r from 0 to 1 gives the corresponding result

$$K_1(t) = -2\int_0^1 (u - U) r \mathrm{d}r = 0. \tag{3.35}$$

It is worth reminding here that U is the average velocity, which has been defined previously, as shown in (3.26). Moving forward, we compute $K_2(t)$, an essential coefficient in (3.31). Its relationship to g_1 and g_2 makes determination non-trivial. Hence, we now employ an alternative method to calculate it. Initially, we intend to utilise the homogenisation principle presented by Duhamel's theorem (Bartels & Churchill 1942). Actually, since g_1 is known (as derived from (3.33a), with the full derivation provided in Appendix C), combining Duhamel's theorem with the superposition principle represents an optimal approach for obtaining $K_2(t)$ without needing to determine the function g_2. Denote $F(r,\ t,\ \tau)$ as the solution of (3.36), along with its initial and boundary conditions

https://doi.org/10.1017/jfm.2026.12134 Published online by Cambridge University Press

$$\frac{\partial F}{\partial t}(r,t,\tau)+[u(r,\tau)-U(\tau)]\,g_1(r,\tau)+K_2(\tau)-\frac{1}{Pe^2}=\frac{1}{r}\frac{\partial}{\partial r}\left(r\frac{\partial F(r,t,\tau)}{\partial r}\right), \tag{3.36a}$$

$$F(r,0,\tau)=0,\quad \frac{\partial F}{\partial r}(0,t,\tau)=\frac{\partial F}{\partial r}(1,t,\tau)=0. \tag{3.36b}$$

In this context, τ acts as a character temporarily treated as a variable for the purpose of substituting τ in $u(r,t)$, $U(t)$, $g_1(r,t)$ and $K(t)$. By decomposing (3.36) into two separate equations and determining the solutions $F_1(r,\tau)$ and $F_2(r,t,\tau)$ for each equation respectively, one can readily acquire the solution $F(r,t,\tau)=F_1(r,\tau)+F_2(r,t,\tau)$ to (3.36*a*) and (3.36*b*):

$$\frac{1}{r}\frac{\partial}{\partial r}\left(r\frac{\partial F_1(r,\tau)}{\partial r}\right)=[u(r,\tau)-U(\tau)]\,g_1(r,\tau)+K_2(\tau)-\frac{1}{Pe^2}, \tag{3.37a}$$

$$\frac{\partial F_2(r,t,\tau)}{\partial t}=\frac{1}{r}\frac{\partial}{\partial r}\left(r\frac{\partial F_2(r,t,\tau)}{\partial r}\right). \tag{3.37b}$$

Furthermore, if we multiply both sides of (3.37*a*) by r and then perform integration from 0 to 1, the expression for $K_2(\tau)$ can be obtained as

$$K_2(\tau)=\frac{1}{Pe^2}-2\int_0^1 r[u(r,\tau)-U(\tau)]g_1(r,\tau)\mathrm{d}r+\left[r\frac{\partial F_1(r,\tau)}{\partial r}\right]_{r=0}^{r=1}. \tag{3.38}$$

To obtain $K_2(\tau)$, we need to solve the last term on the right-hand side of (3.38), which involves the boundary conditions of function F_1. The boundary condition $\partial F(1,t,\tau)/\partial r=0$ necessitates $\partial F_2(1,t,\tau)/\partial r=0$. Otherwise, if $\partial F_2(1,t,\tau)/\partial r\neq 0$, by the superposition $\partial F/\partial r=\partial F_1/\partial r+\partial F_2/\partial r$, this would force $\partial F(1,t,\tau)/\partial r$ to become a non-zero function of t, directly contradicting the original boundary condition. Therefore, we can deduce that $\partial F_1(1,\tau)/\partial r=0$. Then, (3.38) can be rewritten in the following form by replacing τ with t:

$$K_2(t)=\frac{1}{Pe^2}-2\int_0^1 r[u(r,t)-U(t)]g_1(r,t)\mathrm{d}r. \tag{3.39}$$

Under the imposed flow conditions, the convection coefficient vanishes, i.e. $K_1(t)=0$; see (3.35). Consequently, the generalised dispersion model reduces to a simplified form:

$$\frac{\partial C_m}{\partial t}=K_2(t)\frac{\partial^2 C_m}{\partial x_1^2}. \tag{3.40}$$

Next, to derive the average concentration distribution C_m, we firstly define a new variable $\xi=\int_0^t K_2(t')\mathrm{d}t'$ such that the governing equation (3.40) and corresponding initial-boundary conditions transform into

$$\frac{\partial C_m}{\partial \xi}=\frac{\partial^2 C_m}{\partial x_1^2}, \tag{3.41a}$$

$$C_m(x_1,0)=x_s\cdot\delta_{x_s},\quad \delta_{x_s}=\begin{cases}\dfrac{1}{x_s} & x_1\in\left[-\dfrac{x_s}{2},\dfrac{x_s}{2}\right]\\ 0, & \text{others}\end{cases}. \tag{3.41b}$$

https://doi.org/10.1017/jfm.2026.12134 Published online by Cambridge University Press

By applying the Fourier transform to (3.41*a*) and (3.41*b*), we have

$$\tilde{C}_m(\mu, \xi) = \int_{-\infty}^{\infty} x_s \cdot \delta_{x_s} \cdot \mathrm{e}^{-\mathrm{i}\mu\nu} \mathrm{d}\nu \cdot \mathrm{e}^{-\mu^2\xi}. \tag{3.42}$$

Ultimately, the solutions to the system (3.41) are given by the following expression via the inverse Fourier transform:

$$C_m(x_1, \xi) = \frac{1}{2}\left[\mathrm{erf}\left(\frac{\frac{1}{2}x_s + x_1}{2\xi^{\frac{1}{2}}}\right) + \mathrm{erf}\left(\frac{\frac{1}{2}x_s - x_1}{2\xi^{\frac{1}{2}}}\right)\right]. \tag{3.43}$$

Here $\mathrm{erf}(x)$ is the error function.

4. Results and discussions

The primary objective of this investigation is to comprehensively characterise the temporal evolution of solute dispersion in a microtube driven by the MHD-AC-EOF. Consequently, critical parameters governing fluid flow and solute transport must be precisely determined. Based on experiments in microfluidic systems, the radius of the tube R is selected within the range of $10 - 250$ μm (Sparks *et al.* 2003), the fluid density ρ is set to 10^3 kg m^{-3} (Wang *et al.* 2011; Nghe *et al.* 2011) and fluid viscosity η is in the range of $10^{-3} - 2 \times 10^{-3}$ kg m^{-1}s^{-1} (Wang *et al.* 2011; Nghe *et al.* 2011). Based on the works of EOF and MHD (Liu *et al.* 2012; Li & Jian 2017), Helmholtz–Smoluchowski velocity U_{EO} is set to $10^{-5} - 2.5 \times 10^{-4}$ m s^{-1}. Referring to the analysis of solute dispersion in a microchannel by Rana & Murthy (2016*a*,*b*), the constant diffusion coefficient D is taken as $10^{-10} - 10^{-9}$ m^2 s^{-1}, the local concentration C_0 as 10^{-3} mol L^{-1} and the injection band width $\bar{x}_s$ as 10^{-4} m. Additionally, the interface slip coefficient δ is considered to be $0 - 0.5$ μm (Zhu & Granick 2001; Vasista *et al.* 2021), the imposed magnetic field B_0 as $0 - 0.44$ T (Jang & Lee 2000; Xie & Jian 2017; Yang *et al.* 2019). The electrical conductivity σ_e is $2.2 \times 10^{-4} - 10^6$ S m^{-1} (Xie & Jian 2017; Yang *et al.* 2019; Siva *et al.* 2023), where the high conductivity values are set to explore the evolution laws of fluid flow and solute transport across a broad electromagnetic effect parameter range. The relaxation time λ is simulated within a range of 4×10^{-4} s to 5×10^{-3} s. This interval safely aligns with the typical relaxation time domain $10^{-4} - 10^3$ s documented in Bird *et al.* (2001). Crucially, the relaxation time must satisfy the condition $\lambda \leq 2\pi/\bar{\omega}$ (or $De < 2\pi$), ensuring it remains smaller than the oscillating period of the electric field, as stipulated in Bird *et al.* (2001) and Liu *et al.* (2015); thus, the oscillating angular frequency $\bar{\omega}$ is selected within $0.2\pi - 5\pi \times 10^3$ rad s^{-1}. Therefore, the dimensionless parameter values derived from real-world microfluidic system data and used in our simulation are listed in the table 1.

Prior to investigating the solute dispersion under the combined MHD-AC-EOF drive, the accuracy of the analytical solutions from the previous sections must be validated. Figure 2(*a-d*) provides a comparison between the present analytical results of electric potential, velocity, dispersion coefficient and mean concentration distribution with results from existing literature (Soong *et al.* 2010; Liu *et al.* 2012; Li & Jian 2017; Banerjee *et al.* 2021), across varying critical governing parameter values. As evident from figure 2(*a–d*), all sets of results exhibit excellent consistency, which confirms both the reliability of the current model and the precision of the analytical algorithm utilised in this

https://doi.org/10.1017/jfm.2026.12134 Published online by Cambridge University Press

Parameter	Value
Order of the fractional derivative α	0–1
Order of the fractional derivative β	0–1 ($<\alpha$)
Deborah number De	0–1
Debye parameter κ	10–30
Oscillation Reynolds number Re	0–50
Peclet number Pe	50
Hartmann number Ha	0–3
Interface slip coefficient δ	0–0.05
Surface slip-independent zeta potential ζ	0.5
Injection bandwidth x_s	0.019

Table 1. Normalised ranges of major dimensionless parameters.

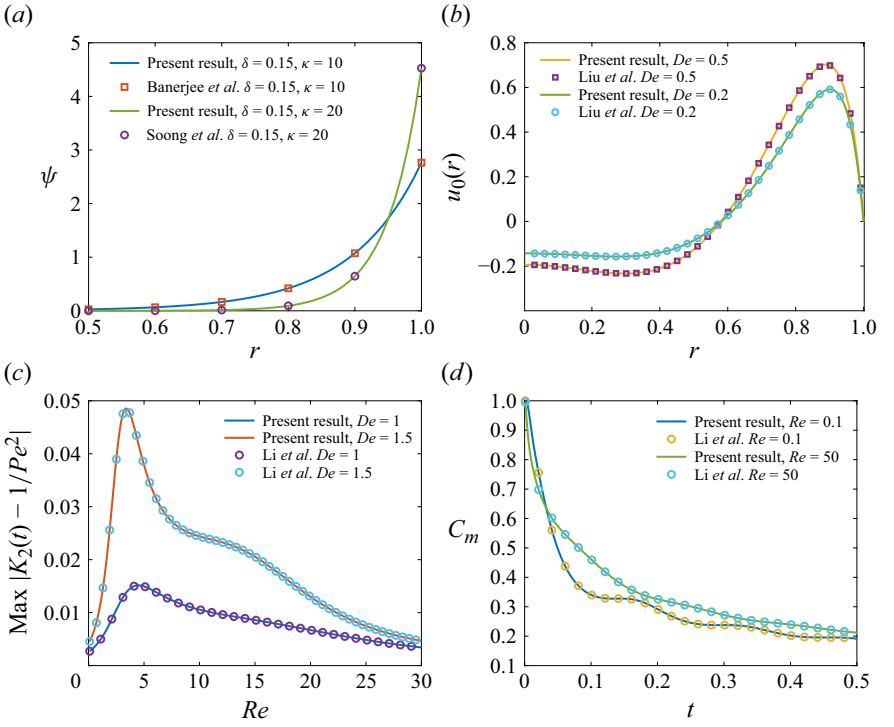


Figure 2. (*a*) Comparison of the present potential distribution with Soong *et al.* (2010), Banerjee *et al.* (2021) for the case of a slip-dependent zeta potential at $\zeta = 1$. (*b*) Comparison of present velocity profiles with Liu *et al.* (2012) at $\alpha = 1$, $\beta = 0$, $\kappa = 20$, $\zeta = 1$, $\delta = 0$, $Re = 10\pi$. (*c*) Comparison of the mean dispersion coefficient between the present study and Li & Jian (2017) at $\alpha = 1$, $\beta = 0$, $\kappa = 10$, $\omega = 20$, $\zeta = 1$, $\delta = 0$. (*d*) Comparison of the mean concentration between the present study and Li & Jian (2017) at $\alpha = 1$, $\beta = 0$, $\kappa = 10$, $\omega = 20$, $De = 1$, $Pe = 50$, $\zeta = 1$, $\delta = 0$, $x_s = 0.019$, $x_1 = 0.005$.

study. Subsequent sections will present a comparative analysis of the effects of major dimensionless parameters on the dispersion coefficient and mean concentration for two flow configurations: AC electro-osmotic-driven flow ($Ha = 0$) and mixed MHD and AC electro-osmotic-driven flow ($Ha \neq 0$).

https://doi.org/10.1017/jfm.2026.12134 Published online by Cambridge University Press

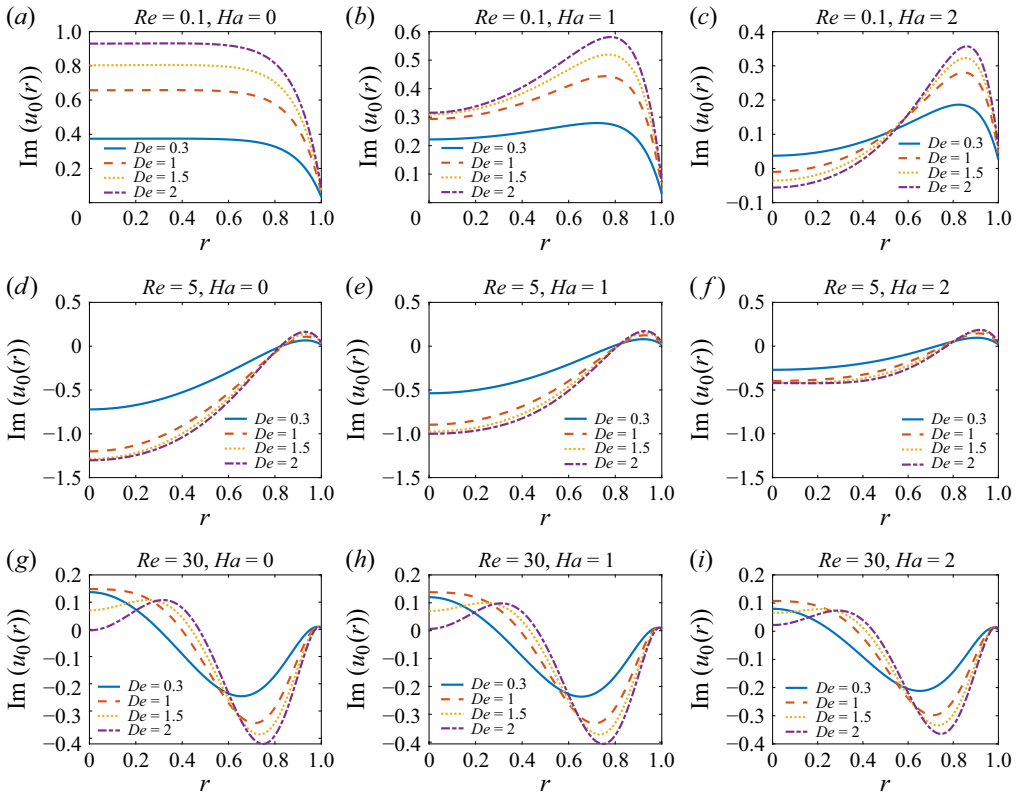


Figure 3. Spatial variation of the imaginary part of the velocity complex amplitude $\mathrm{Im}\{u_0(r)\}$ with r for Deborah number De and Hartmann number Ha at different values of Reynolds number Re ($\kappa = 10$, $\zeta = 0.5$, $\delta = 0.01$, $\alpha = 0.8$, $\beta = 0.4$).

4.1. *Velocity distribution*

This subsection focuses on investigating the rules governing how key parameters affect the velocity distribution, and thus, provides support for the in-depth analysis of the solute dispersion mechanism. First, we aim to analyse the velocity distribution under both pure AC-EOF actuation ($Ha = 0$) and mixed MHD-AC-EOF actuation ($Ha \neq 0$); see figure 3(*a-i*). A broad range of Hartmann numbers ($0 \leq Ha \leq 3$) is employed to explore the underlying mechanism of magnetic field–fluid interaction and reveal the evolution laws under both weak and strong electromagnetic effects. As anticipated, when the Hartmann number (Ha) is set to zero and the oscillation Reynolds number (Re) is small, the velocity profile exhibits a plug-like morphology of classical EOF; see figure 3(*a*). In the presence of a magnetic field ($Ha = 1, 2$), the imaginary part of the velocity complex amplitude begins to decrease and the alteration in the velocity profile becomes more substantial; see figures 3(*b*) and 3(*c*). The underlying cause is that the Lorentz force in the axial direction, with a magnitude of $\sigma_e B_0^2 u_0$ in (3.16), acts as an opposing force, thus leading to the reduction of velocity. Then, as the oscillation Reynolds number Re increases, the influence of the magnetic field on the flow velocity gradually weakens. Although the trend of flow velocity change does not show obvious alteration, it is still observable that the presence of the magnetic field leads to a decrease in the velocity amplitude, as specifically shown in figure 3(*d–f*). Moreover, it can be seen that the continuous increase of Re will result in the magnetic field having a negligible impact on both the trend of velocity change and the

https://doi.org/10.1017/jfm.2026.12134 Published online by Cambridge University Press

amplitude; see figure 3(*g–i*). That is because the dimensionless ratio Ha^2/Re governs the capacity of electromagnetic forces to modulate flow behaviour (Shatrov & Gerbeth 2010). Additionally, we can perceive that an upward trend in Re leads to the emergence of wave-like velocity profiles. For low Reynolds numbers ($Re = 0.1, 5$), the velocity amplitude increases monotonically with De. However, at high $Re = 30$, the velocity field undergoes significant oscillations with large peak-to-valley differences. In this regime, the magnitude of the oscillatory velocity becomes large, but the variation with De is non-monotonic due to the complex coupling effects. This observation can be theoretically elucidated through the following physical mechanisms. In viscoelastic fluids, as the relaxation time increases proportionally with De, the energy-storage capacity of macromolecules is significantly enhanced. Meanwhile, these macromolecules fail to dissipate energy effectively during the oscillation time period (Liu *et al.* 2012; Vasista *et al.* 2021). Consequently, the polymer chains are elongated along the flow direction, which causes a decrease in the cross-sectional area of the polymer molecules. This elongation restricts the molecular flow to the direction of stretching, thereby promoting enhanced shear-thinning behaviour (Colby *et al.* 2007).

Next, to analyse the velocity flow patterns under the combined action of MHD and AC-EOF, we show the absolute amplitude of the cross-sectionally averaged velocity ($|U_1|$) on the plane of the electrokinetic parameter κ and MHD parameter Ha in the contour plot of figure 4. The U_1 is defined below (3.26). It can be observed from figures 4(*a*) and 4(*b*) that the κ-Ha plane can be divided into three regions: at low Ha (<0.5), the region is electric field dominated, where the flow velocity increases with κ; at moderate Ha, the electric force and magnetic forces compete with each other, leading to the flow velocity being sensitive to both κ and Ha while decreasing overall; at high Ha (>1.5 or 2), the region exhibits magnetic field-induced flow restriction, where the flow velocity is significantly suppressed. Furthermore, the flow response of the polymer solution, governed by its viscoelasticity through the Deborah number, differs markedly from Newtonian fluids. At $De = 0.1$, polymer chains respond incompletely to the rapid electric field, limiting velocity at low-to-moderate Ha. However, even at high Ha, increasing the electrokinetic parameter κ still enhances flow, indicating that the field partially overcomes polymeric relaxation lag. In contrast, at $De = 1$, the matched relaxation and field periods enable efficient elastic energy conversion, yielding higher velocities at low-to-moderate Ha before saturation at high Ha. Consequently, a higher De enhances the electric-field-driven flow and elevates the critical Ha for magnetic suppression.

A comparison of figures 4(*b*) and 4(*c*) shows that increasing the Reynolds number (Re) from 5 to 30 markedly reduces the amplitude of cross-sectionally averaged velocity and weakens the magnetic confinement effect. In figure 4(*b*) the flow is highly sensitive to both κ and Ha, as shown by the dense, steep contours and the appearance of a strong confinement zone for $Ha > 2$, indicating distinct flow regimes. In contrast, at $Re = 30$, see figure 4(*c*), the electrokinetic-dominated region extends to higher Ha, the confinement zone shrinks and contours become nearly parallel to the Ha axis. This transition occurs because higher inertial forces at elevated Re enhance momentum transport, partially offsetting the Lorentz force damping and stabilising the tripartite coupling among electric, magnetic and inertial forces, thereby reducing the flow's sensitivity to κ and Ha.

4.2. *Dispersion coefficient* $K_2(t)$

This subsection commences by examining the effects of electro-osmotic and MHD drivings on solute dispersion. To this end, figure 5 presents contour maps of the dispersion coefficient amplitude across the parameter space defined by the electrokinetic parameter

https://doi.org/10.1017/jfm.2026.12134 Published online by Cambridge University Press

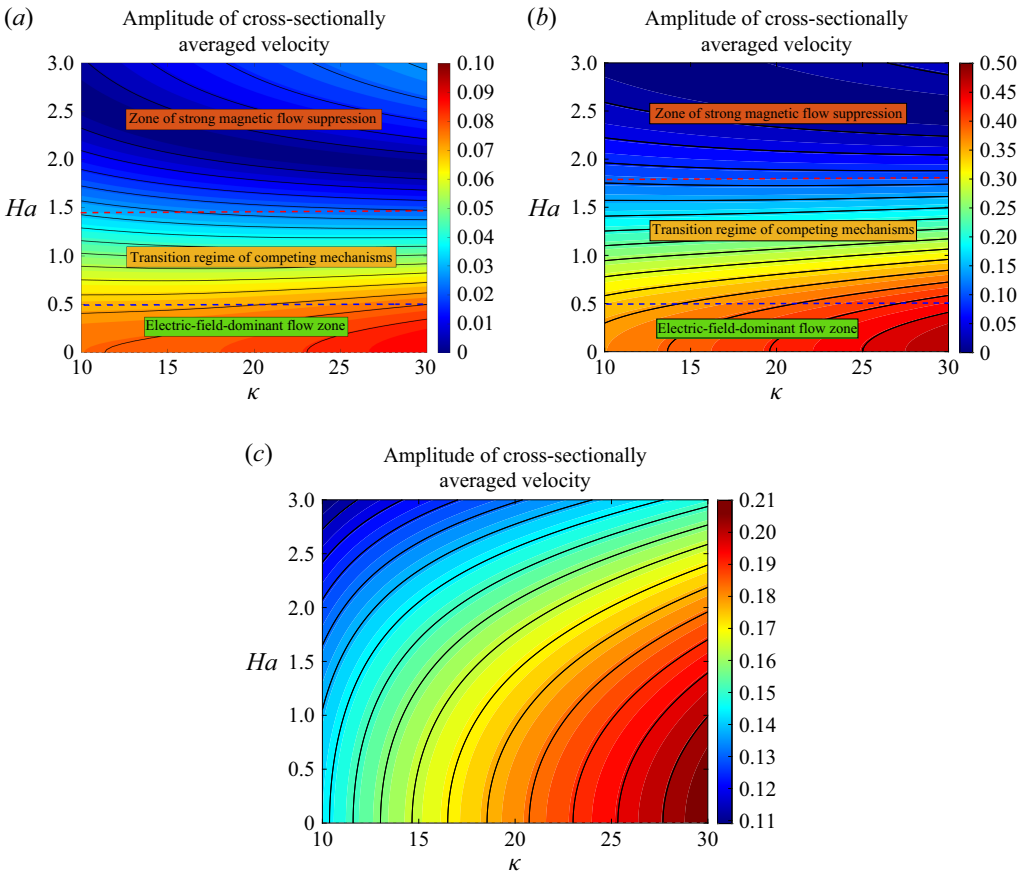


Figure 4. Contour plot of the cross-sectionally averaged velocity for (*a*) $De = 0.1$, $Re = 5$; (*b*) $De = 1$, $Re = 5$; (*c*) $De = 1$, $Re = 30$ under $\alpha = 0.8$, $\beta = 0.4$, $\zeta = 0.5$, $\delta = 0.01$.

κ and the magnetic field parameter Ha. The amplitude of the dispersion coefficient is defined as $(K_2(t))_{amp} = \langle \max(K_2(t)) - \min(K_2(t)) \rangle / 2$, where $\langle \cdot \rangle$ denotes the periodic average. As shown in the figure, the dispersion coefficient amplitude responds distinctly to κ across Ha regimes. In the low-Ha region, the amplitude increases substantially with κ (colour transitions from blue to red) due to weakened Lorentz force damping, which enables effective electrokinetic driving and enhances convective dispersion. This trend reverses in the high-Ha region, where behaviour becomes Re dependent. Under low Re (figures 5*a* and 5*b*), the dominant Lorentz force suppresses flow motion and diminishes the enhancement effect of κ, resulting in limited amplitude growth (the colour shifts to blue). Conversely, at high Re (figure 5*c*), enhanced inertial forces partially compensate for magnetic confinement, maintaining considerable dispersion levels even at high κ.

A comparative analysis of figures 5(*b*) and 5(*c*) further elucidates the distinct dispersion characteristics at different Re. Figure 5(*b*), corresponding to a low-Re regime, displays strongly curved contours and a large dispersion coefficient amplitude. It also exhibits a marked magnetic suppression effect at high Ha, as indicated by the abrupt colour transition toward blue with increasing Ha. In contrast, figure 5(*c*), obtained at high Re, features flattened contours and a significantly lower dispersion amplitude, along with attenuated magnetic suppression under high Ha (manifested as a gradual colour shift). These morphological and amplitude differences stem from enhanced fluid inertia at

https://doi.org/10.1017/jfm.2026.12134 Published online by Cambridge University Press

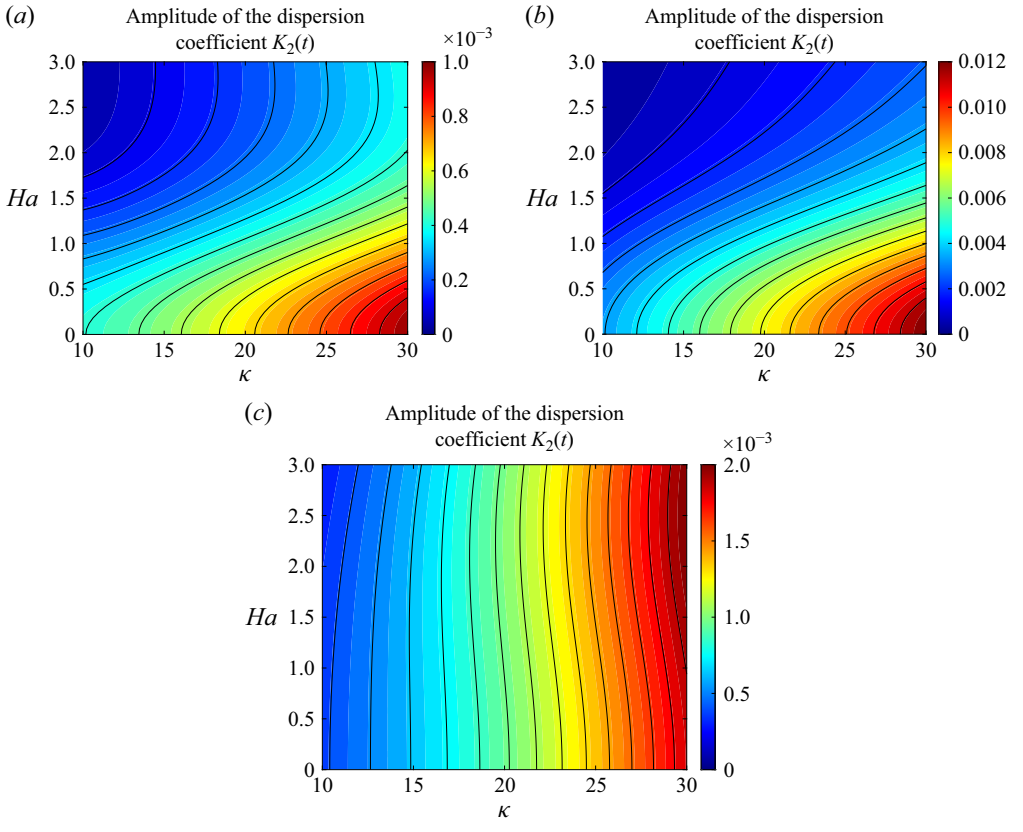


Figure 5. Contour plot of the amplitude of the dispersion coefficient for (*a*) $De = 0.1$, $Re = 5$; (*b*) $De = 1$, $Re = 5$; (*c*) $De = 1$, $Re = 30$ under $\alpha = 0.8$, $\beta = 0.4$, $\zeta = 0.5$, $\delta = 0.01$.

elevated Re, which mitigates magnetic confinement while simultaneously intensifying the κ-driven flow. As a result, electric field effects persist even under high-Ha conditions, leading to clearly divergent dispersion regimes. Additionally, the sensitivity of the dispersion coefficient to the Deborah number (De) is primarily governed by the 'temporal synchronisation' between the electric field and the viscoelastic response of the polymer solution. This is clearly evidenced by comparing figures 5(*a*) and 5(*b*). At $De = 1$, the polymer relaxation time matches the field period, allowing the elastic polymer chains to fully respond and effectively transfer energy. This resonant interaction generates a highly complex oscillatory flow, which dramatically enhances axial dispersion through strong advection–diffusion coupling (figure 5*b*). In contrast, at $De = 0.1$, the rapid field oscillations prevent the polymer chains from responding fully, resulting in weak dispersion effects and generally lower amplitude (figure 5*a*). Therefore, in microfluidic applications such as separation and mixing processes, precise control of these key parameters is essential for optimising the outcome and efficiency.

As mentioned previously, the Reynolds number significantly influences the dispersion coefficient. Therefore, we will next examine the variation of the dispersion coefficient at different Reynolds number values. Figures 6(*a*) and 6(*b*) display the dispersion coefficient under low ($Re < 5$) and high ($Re > 5$) Reynolds number conditions, respectively. The additive contribution of axial diffusion ($1/Pe^2$) has been subtracted from these values, following the data processing approach of Rana & Murthy (2016*a*) (their figures 11–32)

https://doi.org/10.1017/jfm.2026.12134 Published online by Cambridge University Press

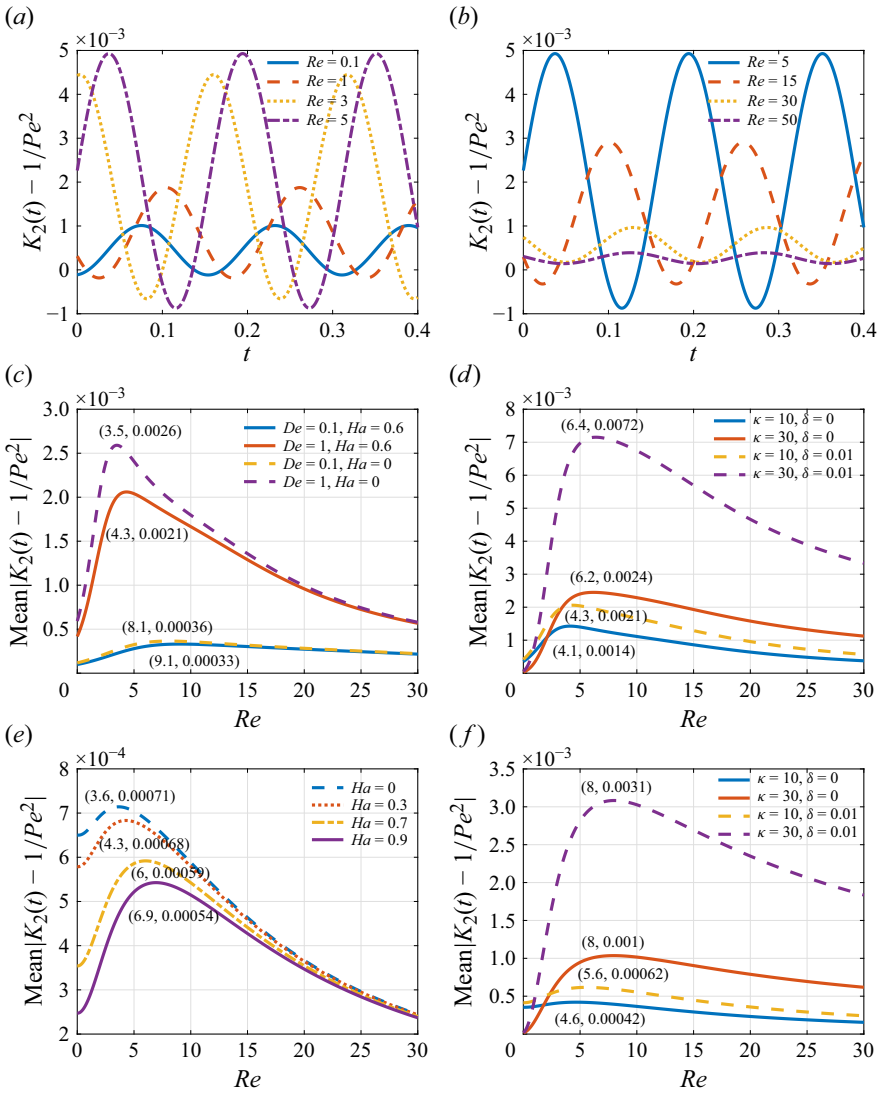


Figure 6. (*a*,*b*) Variations of the dispersion coefficient with t for different values of oscillation Reynolds number Re under $\kappa = 10$, $Ha = 0.6$, $De = 1$, $\omega = 20$, $\zeta = 0.5$, $\delta = 0.01$, $\alpha = 0.8$, $\beta = 0.4$. (*c*,*d*) Mean dispersion coefficient of a fractional Maxwell fluid as a function of the oscillation Reynolds number Re for different parameters under $\omega = 20$, $\zeta = 0.5$, $\alpha = 0.8$, $\beta = 0.4$. (*e*,*f*) Mean dispersion coefficient of a Newtonian fluid as a function of the oscillation Reynolds number Re for different parameters under $\omega = 20$, $\zeta = 0.5$, $\alpha = 1$, $\beta = 1$.

and Sadeghi *et al.* (2020) (their figures 11–16). In the low oscillation Reynolds number regime, viscous and inertial forces operate at comparable magnitudes. As Re increases, the amplitude of the oscillatory inertial force grows significantly and dominates fluid flow, thereby nonlinearly modulating the dispersion coefficient and amplifying the amplitude of $K_2(t) - 1/Pe^2$. Conversely, in the high-Re regime, inertial forces overwhelm viscous forces and their rapid oscillation compresses the growth for the $K_2(t) - 1/Pe^2$ amplitude, manifesting an opposing evolutionary trend. Notably, these findings indicate the existence of a critical oscillation Reynolds number, Re_c, which optimally modulates the amplitude of $K_2(t) - 1/Pe^2$. This observation aligns with the research outcomes presented by Rana &

https://doi.org/10.1017/jfm.2026.12134 Published online by Cambridge University Press

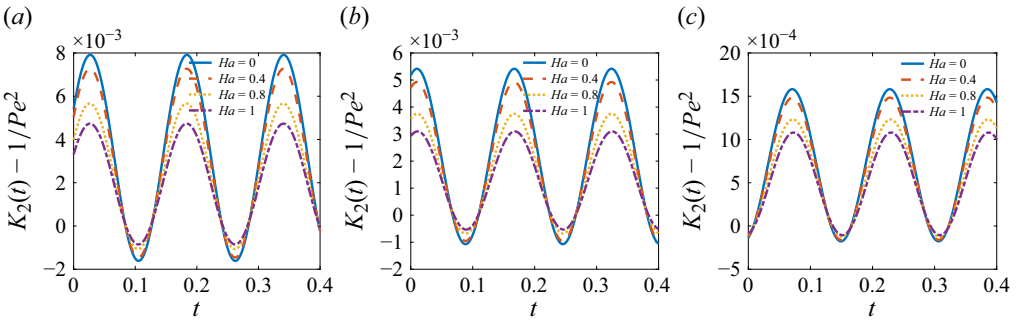


Figure 7. Variations of the dispersion coefficient with different Hartmann numbers Ha for (a) the fractional Maxwell fluid ($\alpha = 0.8$, $\beta = 0.2$), (b) the classical Maxwell fluid ($\alpha = 1$, $\beta = 0$), (c) the Newtonian fluid ($\alpha = 1$, $\beta = 1$) under $\kappa = 10$, $Re = 5$, $De = 1$, $\omega = 20$, $\zeta = 0.5$, $\delta = 0.01$.

Murthy (2016*b*) and Li & Jian (2017). This critical value serves as a pivotal threshold, demarcating the transition between the two disparate response patterns of $K_2(t) - 1/Pe^2$ to changes in Re. Consequently, we need to analyse the influence of relevant parameters on the critical oscillation Reynolds number. Figures 6(*c*), 6(*d*), 6(*e*) and 6(*f*) illustrate the variation of the mean dispersion coefficient with Re for the fractional Maxwell fluid and the Newtonian fluid over the time interval $0 - 5$, respectively. For both fluid models, the mean dispersion coefficient exhibits a unimodal trend of initial increase followed by decrease with Re, corresponding to a well-defined critical Reynolds number Re_c: when $Re < Re_c$, inertial effects enhance transverse mixing of fluid elements, thereby increasing the dispersion coefficient; when $Re > Re_c$, inertia dominates and regularises the flow field, causing the dispersion coefficient to decay with further increase in Re. Notably, Re_c decreases with increasing Deborah number De, while it increases with a larger Hartmann number Ha, Debye parameter κ and slip length δ. For the fractional Maxwell fluid, the Deborah number De characterises its viscoelasticity: a higher De suppresses inertial mixing at lower Re, thereby reducing Re_c. In contrast, the Newtonian fluid, lacking viscoelasticity, exhibits a generally higher Re_c under the same Ha, κ and δ conditions. Furthermore, viscoelasticity amplifies the deformation of fluid elements and enhances mixing, leading to a considerably higher peak dispersion coefficient for the fractional Maxwell fluid.

Figure 7 illustrates the influence of the Hartmann number Ha on $K_2(t) - 1/Pe^2$ under three fluid models, characterised by different parameter combinations: the fractional Maxwell model (FMM) ($\alpha = 0.8$, $\beta = 0.2$), the classical integer-order Maxwell model ($\alpha = 1$, $\beta = 0$) and the Newtonian fluid model ($\alpha = 1$, $\beta = 1$). We find that the amplitude of the dispersion coefficient for FMM is the largest, compared with that of the classical integer Maxwell model and the Newtonian fluid model. This phenomenon can be attributed to the distinct values of fractional parameters, which modulate the relative contributions of viscous and elastic behaviours within the fractional viscoelastic model. Specifically, under the current parameter regime ($\alpha = 0.8$, $\beta = 0.2$), the elastic component exerts a dominant influence, significantly intensifying solution convection and subsequently facilitating the dispersion process. The dispersion coefficients for other values of the fractional parameters are presented in figure 8. It can be observed that as the fractional parameters α and β increase, the amplitude of the dispersion coefficient gradually decreases. The reason is that increasing α and β leads to reductions in both velocity magnitude and gradients, rendering the velocity field more uniform. Such uniformity weakens dispersion and decreases the magnitude of the dispersion coefficient.

https://doi.org/10.1017/jfm.2026.12134 Published online by Cambridge University Press

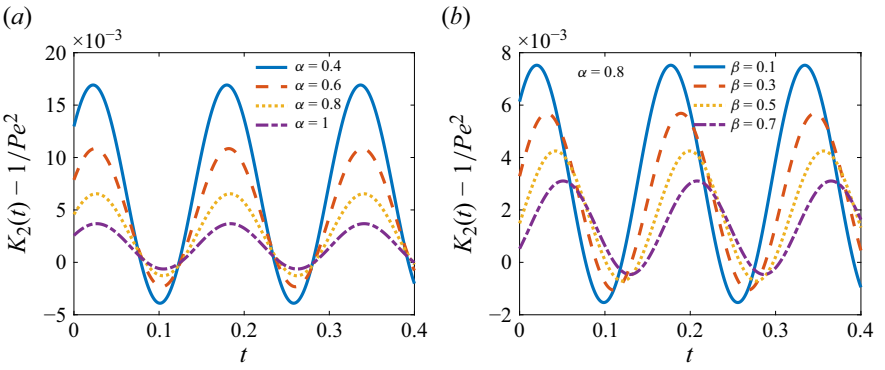


Figure 8. Variations of the dispersion coefficient with t for (a) different fractional parameters α and (b) different fractional parameters β under $\kappa = 10$, $Re = 5$, $De = 1$, $\omega = 20$, $Ha = 0.6$, $\zeta = 0.5$, $\delta = 0.01$.

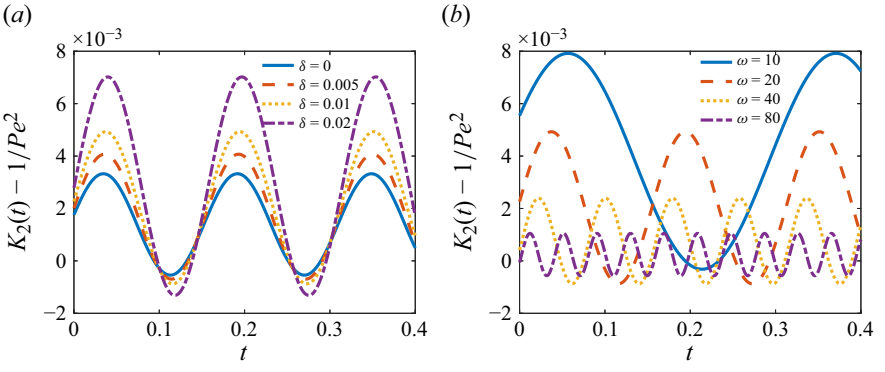


Figure 9. Variations of the dispersion coefficient with t for (a) different slip lengths δ (with $\omega = 20$) and (b) different oscillation frequencies ω (with $\delta = 0.01$ at $\kappa = 10$, $De = 1$, $Re = 5$, $Ha = 0.6$, $\zeta = 0.5$, $\alpha = 0.8$, $\beta = 0.4$.

The impacts of the remaining parameters (slip length δ and oscillation frequency ω) on the dispersion coefficient are comprehensively illustrated in figure 9. It is crucial to emphasise that the degree of dispersion is predominantly governed by the relative significance of the flow velocity magnitude and the configuration of the flow velocity profile. As observed in figure 9(a), an increase in the slip coefficient leads to a higher amplitude of the dispersion coefficient. The underlying mechanisms are as follows, (i) An increased slip coefficient accelerates the flow near the channel wall, bringing its velocity closer to that in the central region and thus disturbing the uniformity of the velocity distribution. (ii) Owing to the interdependence between the slip coefficient and the flow potential, a larger slip coefficient elevates the potential, resulting in greater flow velocity and intensified convective effects. Figure 9(b) illustrates the evolution of dispersion coefficient for specific values of ω. Evidently, as ω increases, the amplitude of the dispersion coefficient decreases accordingly. This phenomenon can be attributed to the fact that a higher ω indicates the period of the applied electric field is significantly shorter than the diffusion time scale. Consequently, the more rapid oscillation of the applied electric field severely restricts the effective time available for solute transport.

https://doi.org/10.1017/jfm.2026.12134 Published online by Cambridge University Press

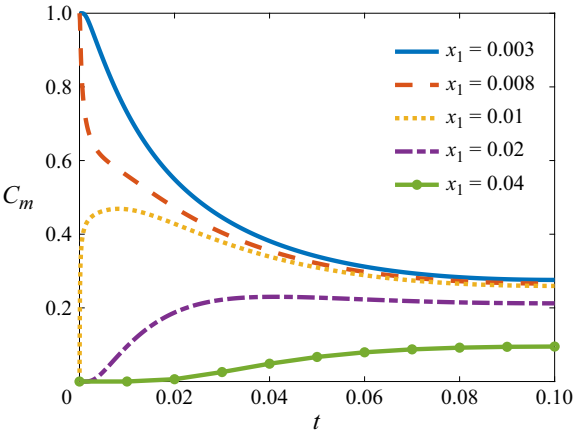


Figure 10. The evolution of the concentration distribution at different positions over time with $Pe = 50$, $\kappa = 10$, $Re = 5$, $De = 1$, $Ha = 0.6$, $\zeta = 0.5$, $\omega = 20$, $\delta = 0.01$, $\alpha = 0.8$, $\beta = 0.4$, $x_s = 0.019$.

4.3. *Mean concentration* $C_m(x_1, t)$

In this subsection we analyse the evolution of the mean concentration distribution C_m with different parameters. As shown in (3.43), the mean concentration distribution is related to the dispersion coefficient $K_2(t)$ through the parameter ξ. Thus, parameters that influence $K_2(t)$ should also be considered for their impacts on the mean concentration. First, the evolution of the mean concentration at different spatial positions x_1 (the formal definition of this quantity can be found in (3.26)) over time with an injection bandwidth of $x_s = 0.019$ is illustrated in figure 10. Analysis indicates that for $x_1 = 0.003$ and 0.008, C_m undergoes monotonic decay over time. In contrast, when $x_1 = 0.01$, 0.02 and 0.04, C_m first increases and then decreases with time t, and the inflection point between these two trends occurs near the boundary of the solute injection region ($|x_1| \approx x_s/2$). A closer examination reveals that as x_1 approaches $x_s/2$, C_m decreases monotonically. Conversely, when $x_1 > x_s/2$, C_m follows a rise-decay pattern, with the peak concentration decreasing as the magnitude of x_1 increases. For cases where $|x_1|$ is substantially distant from $x_s/2$, C_m exhibits a delay in increasing from zero, which indicates that the solute requires a certain period of time to reach the target location from the injection point through transport processes including diffusion, advection and dispersion.

We next analyse the effect of a magnetic field on solute dispersion in AC-EOF driven systems. Recall that $Ha = 0$ corresponds to the absence of a magnetic field (pure AC-EOF), whereas a finite Ha introduces an additional MHD mechanism via the Lorentz force. Figure 11 presents the mean concentration contours at fixed times. It directly illustrates the magnetic field regulation on solute spatial distribution. At early times ($t = 0.005$), the solute is highly concentrated near the centre $x_1 = 0$. A higher Ha indicates a stronger magnetic field. It confines the solute to a narrower central region and yields a sharper concentration peak. As time evolves from $t = 0.02$ to 0.5, the concentration gradually broadens and homogenises. This process is significantly delayed at larger Ha. Strong Lorentz forces suppress radial fluid motion. They sustain steeper concentration gradients and prolong the transient dispersion phase. To further complement the spatial perspective, figure 12 displays the temporal evolution of mean concentration at fixed Hartmann numbers. Figure 12(*a–c*) shows the spatial distribution of mean concentration at various times. Under pure AC electro-osmotic driving with $Ha = 0$, the concentration peak flattens and spreads more rapidly. This behaviour indicates enhanced dispersion.

https://doi.org/10.1017/jfm.2026.12134 Published online by Cambridge University Press

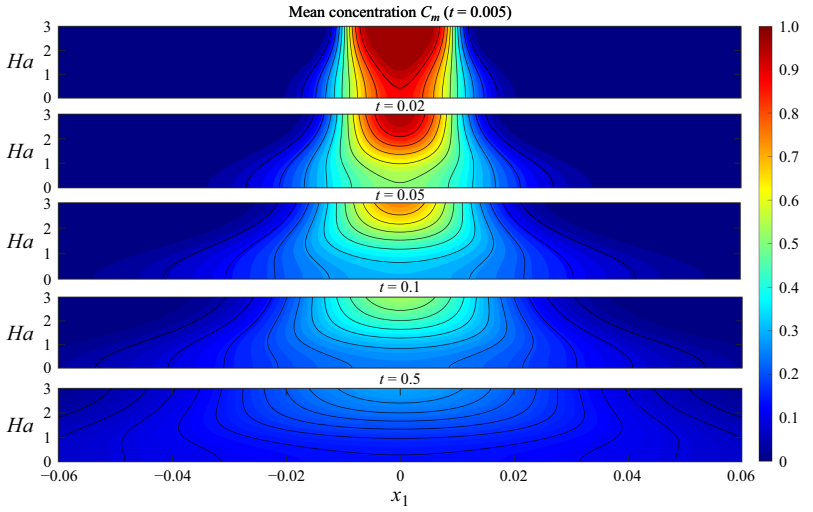


Figure 11. Mean concentration contours at various times for different Hartmann numbers with $Pe = 50$, $\kappa = 10$, $Re = 5$, $De = 1$, $\omega = 20$, $\zeta = 0.5$, $\delta = 0.01$, $\alpha = 0.8$, $\beta = 0.4$, $x_s = 0.019$.

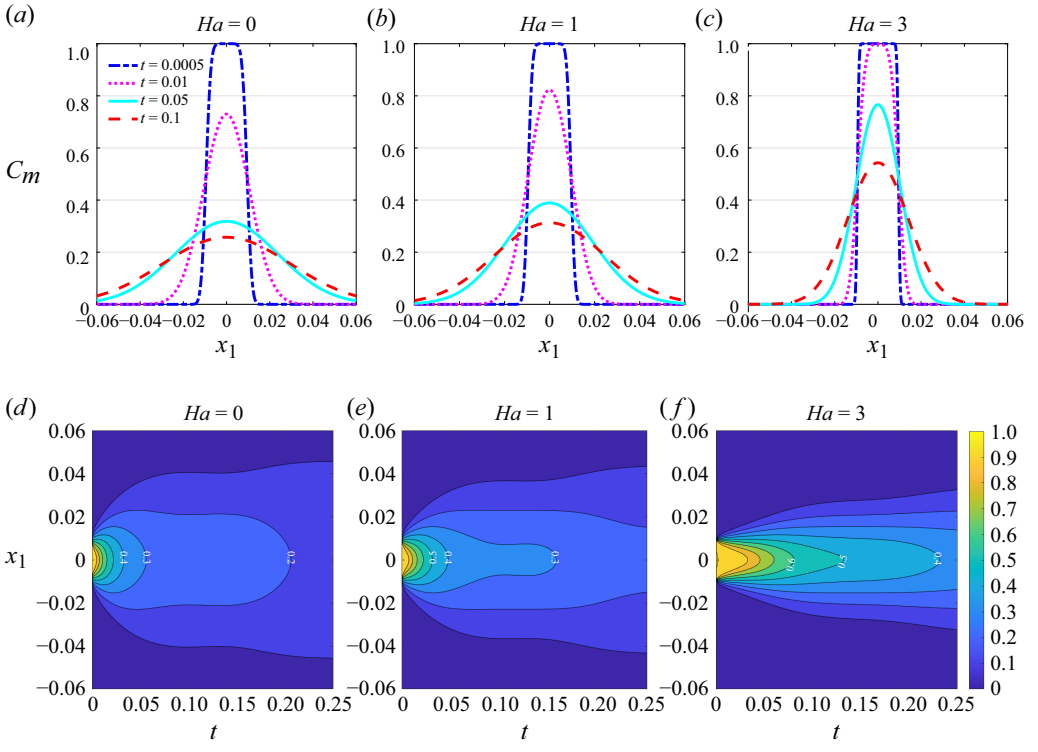


Figure 12. (*a–c*) Variation of the mean concentration along the axial distribution with different Hartmann numbers. (*d–f*) Mean concentration contours of solute with different Hartmann numbers at $Pe = 50$, $\kappa = 10$, $Re = 5$, $De = 1$, $\omega = 20$, $\zeta = 0.5$, $\delta = 0.01$, $\alpha = 0.8$, $\beta = 0.4$, $x_s = 0.019$.

In contrast, increasing *Ha* attenuates dispersion. It notably prolongs the initial transient phase and delays homogenisation. Figure 12(*d–f*) offers a clearer comparison through concentration profiles and contours. In the absence of a magnetic field with $Ha = 0$,

https://doi.org/10.1017/jfm.2026.12134 Published online by Cambridge University Press

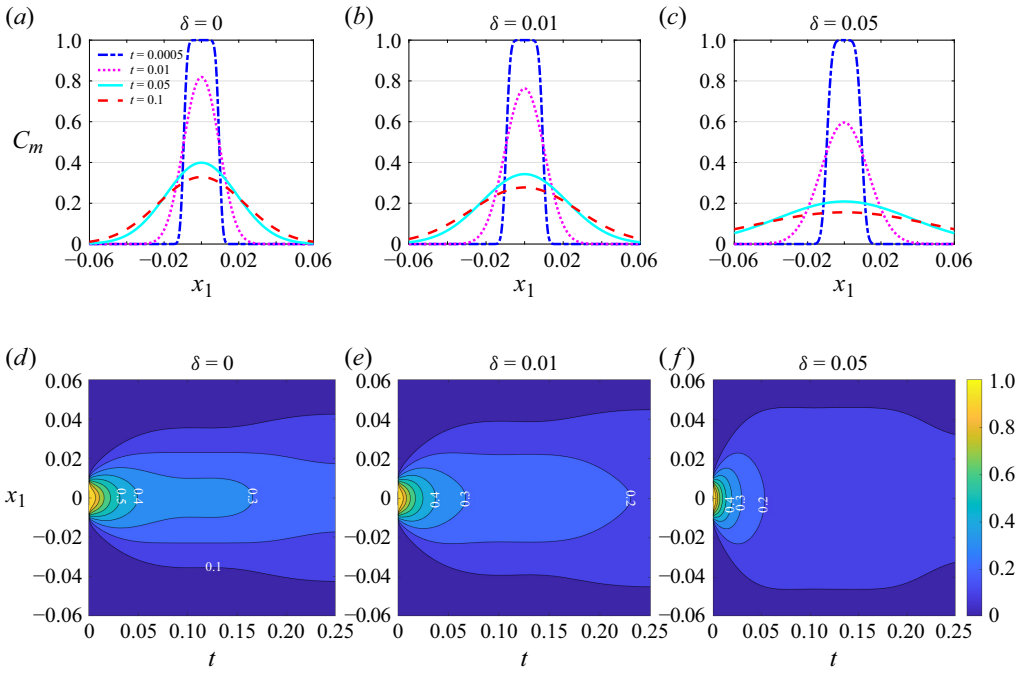


Figure 13. (*a–c*) Variation of the mean concentration along the axial distribution with different slip lengths. (*d–f*) Mean concentration contours of solute with different slip lengths at $Pe = 50$, $\kappa = 10$, $Re = 5$, $De = 1$, $\omega = 20$, $Ha = 0.6$, $\zeta = 0.5$, $\alpha = 0.8$, $\beta = 0.4$, $x_s = 0.019$.

AC-EOF induces strong convective transport. This leads to fast dispersion and early homogenisation. Applying a magnetic field suppresses EOF through Lorentz forces. It weakens convection and retards homogenisation. Under strong magnetic fields, flow velocity is significantly reduced. Concentration gradients can be sustained for extended periods without full homogenisation. Together, figures 11 and 12 provide a comprehensive picture of magnetic field effects: with the electro-osmotic effect held constant, higher *Ha* constrains the solute near the centre and slows down dispersion, while lower *Ha* promotes uniform radial distribution and faster homogenisation.

Figure 13(*a–f*) illustrates the influence of the interfacial slip coefficient on the mean concentration distribution. The presence of slip accelerates initial solute dispersion and reduces the time required for full homogenisation. This behaviour stems from slip-enhanced boundary velocity profiles. Through the slip-amplified zeta potential, convective transport is intensified and velocity non-uniformity increased, thereby expediting solute homogenisation.

The FMM can reduce to either the classical Maxwell model or the Newtonian fluid model depending on the fractional parameters, making a comparative analysis of their dispersion behaviours necessary. As shown in figure 14, compared with the integer-order Maxwell and Newtonian models, the FMM exhibits a rapid initial response and enhanced dispersion depth due to its long-range memory and multi-scale characteristics, leading to the fastest peak decay and the lowest equilibrium concentration. However, its long-tail relaxation prolongs the time to reach steady state. The classical Maxwell model achieves quick elastic–viscous balance via exponential relaxation, resulting in efficient early stage dispersion, moderate final mixing and the shortest stabilisation time. In contrast, the Newtonian fluid, lacking elasticity and memory, shows the slowest decay and

https://doi.org/10.1017/jfm.2026.12134 Published online by Cambridge University Press

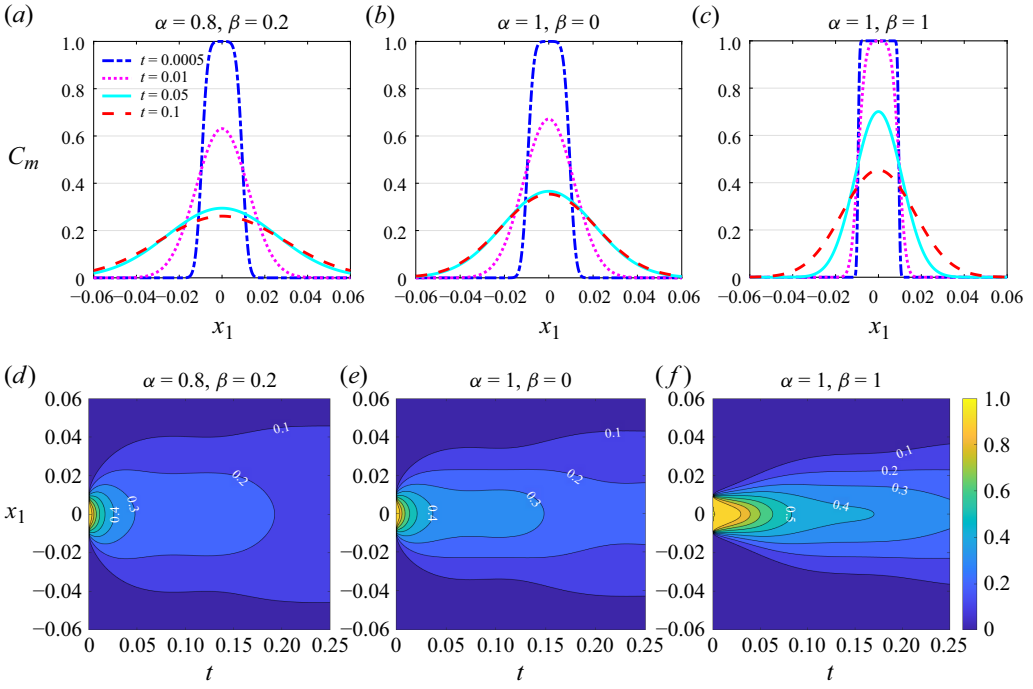


Figure 14. (*a–c*) Variation of the mean concentration along the axial distribution with different fractional parameters. (*d–f*) Mean concentration contours of solute with different fractional parameters at $Pe = 50$, $Re = 5$, $De = 1$, $\kappa = 10$, $\omega = 20$, $Ha = 0.6$, $\zeta = 0.5$, $\delta = 0.01$, $x_s = 0.019$.

least dispersion. This mechanism reflects the crucial influence of the relaxation behaviour of the microscopic structure on the macroscopic solute transport in multi-field coupling scenarios, ranging from simple viscous fluids to complex viscoelastic fluids.

The effect of fractional parameters on the mean concentration distribution is given in figures 15(*a*) and 15(*b*). It can be observed that when either fractional parameter β (or α) is held constant, the peak mean concentration increases as α (or β) increases. A higher α enhances the fluid's sensitivity to high-frequency oscillations in the AC electric field, reducing phase lag and improving particle tracking. This promotes directed migration and aggregation under periodic forcing. Meanwhile, an increase in β intensifies the stress memory effect, effectively suppressing random diffusion. Thus, raising both α and β amplifies the concentration peak and attenuates dispersion. To quantitatively evaluate the axial homogenisation of solutes under hybrid MHD-AC-EOF over time, we introduce a modified version of the concentration difference percentage index used in previous studies (Wu & Chen 2014; Reshadi & Saidi 2019). The index R_a is defined as

$$R_a(t) = \frac{\max\left[C_m(x_1, t)\right] - \min\left[C_m(x_1, t)\right]}{C_m(x_1, t)|_{x_1=0,\, t=t_0}} \times 100\,\%. \tag{4.1}$$

Here R_a represents the ratio of the maximum variation in the axially mean concentration over a predefined distance ($x_1 \in [-0.06, 0.06]$) to the concentration at the centroid of the solute band at a given time, thus serving as a crucial metric for evaluating the degree of axial uniformity of the solute. As demonstrated in figures 15(*c*) and 15(*d*), R_a for different fractional parameters exhibits an oscillatory decline over time, indicating that the axial distribution of the solute gradually achieves uniformity. Moreover, an increase

https://doi.org/10.1017/jfm.2026.12134 Published online by Cambridge University Press

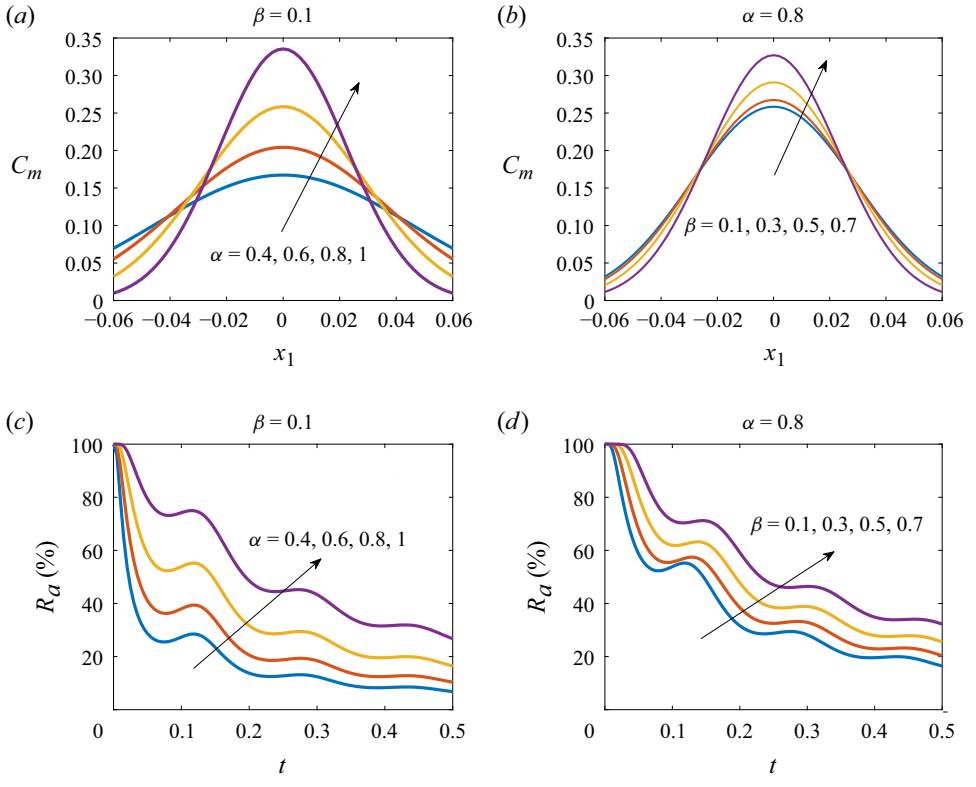


Figure 15. (*a*,*b*) Variation of the mean concentration along the axial distribution with different fractional parameters α and β at $t = 0.1$. (*c*,*d*) The percentage of axial concentration difference varies as a function of the fractional parameters α and β, under $Pe = 50$, $\kappa = 10$, $Re = 5$, $De = 1$, $\omega = 20$, $\delta = 0.01$, $Ha = 0.6$, $\zeta = 0.5$, $x_s = 0.019$.

in the fractional parameters α and β leads to an elevation in R_a, signifying greater axial non-uniformity of the solute concentration.

Figure 16 displays contour plots of the mean concentration distribution at various oscillation Reynolds numbers Re. Below the critical value, the concentration gradient decreases gradually, which leads to a more uniform solute distribution and reduces the time required to reach steady state. At $Re = 5$, the concentration profile is nearly homogeneous throughout the entire domain, indicating highly effective dispersion. Above Re_c ($20 \leq Re \leq 50$), increases in Re sharpen concentration gradients and amplify solute non-uniformity, reflecting a reduction in dispersion efficacy. This behaviour occurs because, at low Re, electromagnetic and viscous forces act together to enhance dispersion. At high Re, inertial forces dominate and nonlinear interactions between electromagnetic and inertial effects reverse the trend in concentration gradient, thereby increasing the spatial heterogeneity of the solute distribution.

Figure 17 illustrates the mean concentration contours of solute at different Deborah numbers De. Clearly, an increase in De results in a reduction in C_m, which can be attributed to the enhanced convective effects that render the dispersion process more pronounced. By comparing the concentration distribution characteristics of the fractional Maxwell fluid ($De \neq 0$) and the Newtonian fluid ($De = 0$), it is found that the solute dispersion rate in the fractional Maxwell fluid is faster. This difference is directly related to the inherent elastic effect of viscoelastic fluids. The contours of mean concentration with

https://doi.org/10.1017/jfm.2026.12134 Published online by Cambridge University Press

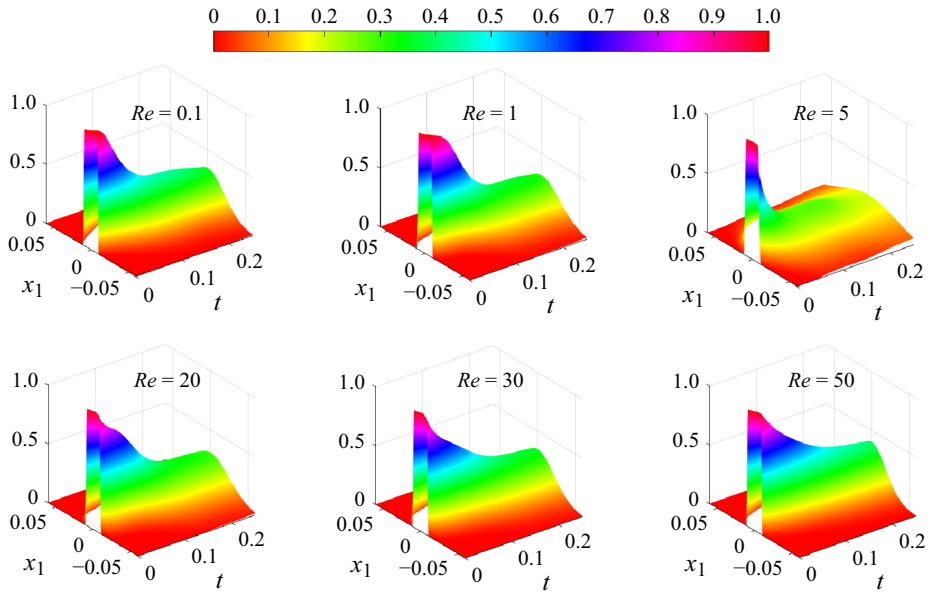


Figure 16. Surface plots of the mean solute concentration for different oscillation Reynolds numbers Re at $\alpha = 0.8$, $\beta = 0.4$, $Pe = 50$, $\kappa = 10$, $De = 1$, $\omega = 20$, $Ha = 0.6$, $\zeta = 0.5$, $\delta = 0.01$, $x_s = 0.019$.

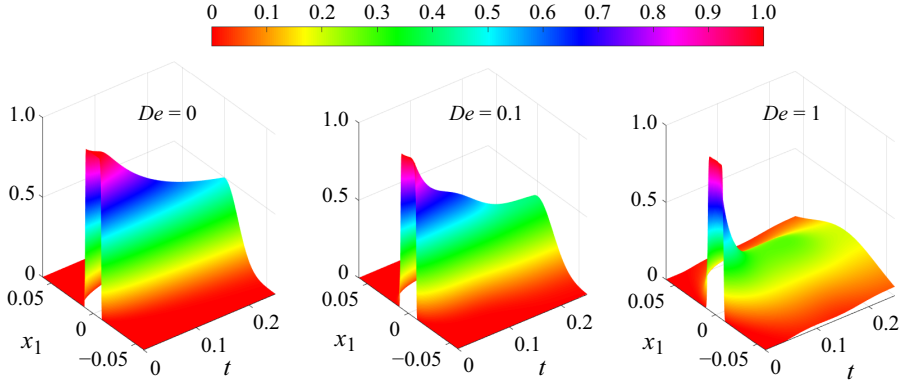


Figure 17. Surface plots of the mean solute concentration for different Deborah numbers De at $\alpha = 0.8$, $\beta = 0.4$, $Pe = 50$, $\kappa = 10$, $Re = 5$, $\omega = 20$, $Ha = 0.6$, $\zeta = 0.5$, $\delta = 0.01$, $x_s = 0.019$.

different oscillation frequencies ω are given in figure 18. When the frequency of the AC electric field is low, the solute has sufficient time to respond to the electric field actuation, accelerating the dispersion process and causing the concentration distribution to rapidly approach uniformity. Conversely, under high-frequency conditions, solute migration fails to keep pace with the rapid oscillations of the electric field, giving rise to periodic concentration fluctuations and a notable enhancement of the concentration gradient.

5. Conclusion

An outstanding challenge in microfluidic transport is the accurate modelling of solute dispersion in viscoelastic fluids under multiphysics fields, where key interfacial phenomena such as hydrodynamic slip and zeta potential coupling are critical. The

https://doi.org/10.1017/jfm.2026.12134 Published online by Cambridge University Press

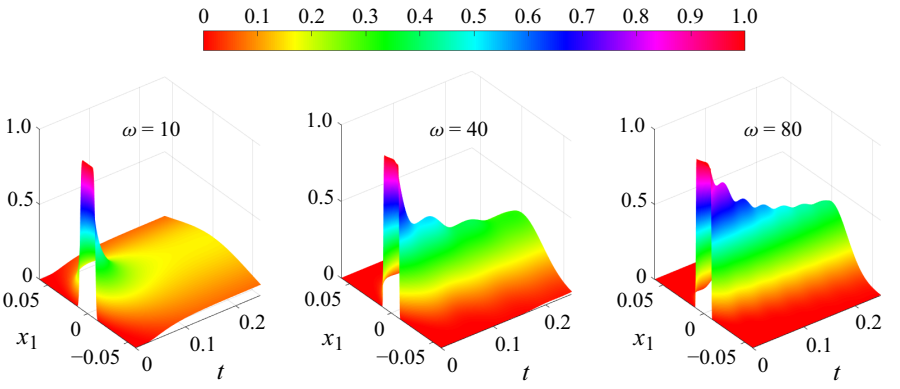


Figure 18. Surface plots of the mean solute concentration for different oscillation frequencies ω at $Re = 5$, $\alpha = 0.8$, $\beta = 0.4$, $Pe = 50$, $\kappa = 10$, $De = 1$, $Ha = 0.6$, $\zeta = 0.5$, $\delta = 0.01$, $x_s = 0.019$.

omission of these effects has hindered the development of high-performance mixers and separators. To address this, we introduce a unified theoretical framework that integrates these previously neglected phenomena. Our model provides analytical solutions capable of capturing the full spatiotemporal transport dynamics, thereby establishing a foundational tool for the predictive design of complex microfluidic systems. We demonstrate that the strategic application of a reverse Lorentz force via a magnetic field effectively suppresses solute dispersion in AC-EOF by flattening the underlying velocity profile. This approach proves most effective when the EDL is thick (i.e. for small values of κ). Our results confirm the cross-system universality of a fundamental principle: as concurrently revealed by Samuel *et al.* (2025) for EOF driven flows, employing an opposing pressure gradient to modulate flow morphology constitutes a robust and universal strategy for minimising solute dispersion.

The key findings of this study show that while the MHD suppression of solute dispersion in polymer solutions aligns with observations in both Newtonian (Das *et al.* 2024*b*) and non-Newtonian systems (Sen *et al.* 2025), the viscoelasticity of these solutions induces a distinct coupled-field response. Specifically, at elevated Deborah numbers (De), electric-field-induced polymer chain stretching and alignment enhance electrokinetic flow, intensify axial dispersion and increase the critical Hartmann number (Ha) needed for MHD suppression. Moreover, the dispersion response to the electrokinetic parameter (κ) exhibits significant sensitivity to Ha. Under low-Ha conditions, the dispersion amplitude increases with κ, indicating electrokinetic dominance. In contrast, at high Ha, the behaviour transitions to a Reynolds number (Re)-dependent regime: Lorentz forces dampen the flow and diminish the effect of κ at low Re, whereas at high Re, inertial forces partially overcome the MHD suppression, thereby sustaining a higher dispersion level.

Furthermore, this study broadens the scope of investigation by exploring the effect of flow inertia on dispersion behaviour across an extended Re range of 1–30, which goes beyond the limited low-Re framework (0.1–2) typically covered in existing literature (Reshadi & Saidi 2019; Das *et al.* 2024*b*; Sen *et al.* 2025). Due to their constrained Re intervals, prior studies could only report a monotonic trend of decreasing dispersion with increasing Re. In contrast, our work, spanning a wider Re range, reveals a key nonlinear feature: there exists a critical Re_c value below which the dispersion coefficient increases with Re and above which it decreases. This critical Re_c is collectively influenced by multiple parameters, including Ha, De, κ and slip coefficient (δ).

https://doi.org/10.1017/jfm.2026.12134 Published online by Cambridge University Press

Our study also advances microfluidic transport analysis by integrating interfacial slip and its electrokinetic coupling with the zeta potential, extending beyond the conventional no-slip paradigm. Results indicate that the slip-dependent zeta potential model significantly enhances near-wall electrokinetic fields and flow velocities, exacerbating velocity profile non-uniformity and thereby intensifying global solute dispersion. Combined with prior research showing that 'asymmetric channel-wall zeta potential' (Das *et al.* 2024*b*) and 'interfacially grafted PELs' (Reshadi & Saidi 2019; Sadeghi *et al.* 2020) also enhance dispersion, our findings position the active regulation of microchannel wall properties as a novel approach for controlling axial solute dispersion in microfluidic systems.

Although this study systematically analyses solute dispersion in MHD and AC-EOF, certain limitations remain, such as the idealised circular tube geometry and the focus on dilute single-solute systems. Despite these, this work advances the fundamental understanding of solute transport in microfluidic systems by elucidating the coupled effects of MHD and EOF. It reveals how key dimensionless parameters, such as the Hartmann number, electrokinetic parameter and Reynolds number, govern flow patterns and dispersion characteristics, providing theoretical insights and practical guidance for electromagnetically driven microfluidic devices, including lab-on-a-chip systems, targeted drug delivery and micromixers. Future work will aim to overcome the above limitations and establish a quantitative model correlating the Reynolds number, Hartmann number and electrokinetic parameter to develop a generalised stability criterion, ultimately supporting precise flow control in such devices.

Funding. This work was supported by the National Natural Science Foundation of China (NSFC, Grant Nos. 12402300, 12172197 and 12171284) and the Natural Science Foundation of Shandong Province (Grant Nos. ZR2024QA160 and ZR2025MS35).

Declaration of interests. The authors report no conflict of interest.

Appendix A

This paper studies solute dispersion in aqueous solutions of hydroxyethyl cellulose (HEC) and xanthan gum (XG). These polymers are ideal for microfluidic applications owing to their water solubility, pseudoplasticity and stability. Such properties aid in flow regulation and help minimise unintended variations in dispersion. In microfluidic systems, HEC and XG solutions are commonly employed to control the transport and dispersion of solutes, such as drug molecules, through viscosity modulation. Therefore, accurate rheological modelling is essential for predicting and managing solute behaviour in processes like mixing and separation. This section aims to establish appropriate viscoelastic models for these solutions to support subsequent analysis of solute diffusion and transport in microchannels.

A.1. *Rheological properties of HEC and XG aqueous solutions*

Experimental studies (Dinic & Sharma 2020; Cao & Kraume 2022) have shown that the frequency responses of aqueous solutions of HEC and XG adhere to a power-law relationship. The macroscopic viscoelastic phenomena observed in polymers, such as stress relaxation, originate from the motion of molecular segments. This classic concept is extensively detailed in Ferry (1980). Specifically, the viscoelastic storage modulus and loss modulus exhibit a frequency-dependent behaviour described by $G'(\omega) \sim \omega^{\alpha}$, $G''(\omega) \sim \omega^{\beta}$. However, traditional rheological models such as the Maxwell

https://doi.org/10.1017/jfm.2026.12134 Published online by Cambridge University Press

model and the Kelvin–Voigt model cannot adequately capture such power-law characteristics.

Although additional mechanical elements can be added in series or parallel to the basic Maxwell or Kelvin–Voigt elements (Tschoegl 1989) to introduce more relaxation modes and enable the modelling of power-law materials, this method often requires an excessive number of mechanical elements when dealing with many complex solutions. This not only increases model complexity but also raises computational demands, making it infeasible in practical modelling scenarios. Furthermore, in models with a finite set of relaxation modes, the values of the fitted parameters are highly sensitive to the time scale of the experimental data used for fitting. As a result, the model parameters obtained through this process often lack clear physical significance (Kollmannsberger & Fabry 2011). The fractional constitutive model integrated with spring-pot mechanical elements is capable of providing a natural and quantitative description of the power-law behaviour commonly observed in experiments with only a few constitutive parameters. Therefore, in this paper we use the fractional Maxwell viscoelastic model derived from the fractional stress–strain relationship to quantitatively describe the power-law rheological behaviour exhibited by such solutions.

A.2. *Fractional Maxwell viscoelastic model*

The classical linear viscoelastic Maxwell model has the following integral form:

$$\sigma(t) = G_0 \int_{-\infty}^{t} \mathrm{e}^{-\frac{t-t'}{\lambda}} \frac{\mathrm{d}\gamma(t')}{\mathrm{d}t'} \mathrm{d}t'. \tag{A1}$$

In this equation, $G(t) = G_0 \mathrm{e}^{-\frac{t}{\lambda}}$ is defined as the relaxation modulus, which describes the stress response to an instantaneous deformation jump. Notably, this integral form is a specific instance of the Boltzmann integral and is characterised by exponential decay. It is widely used to characterise the linear viscoelastic deformation of complex materials. However, for materials exhibiting different forms of memory fading behaviour, such as some polymer solutions with power-law decay behaviour (e.g. the HEC solution and XG aqueous solution considered in this study), polymer gels (Martin *et al.* 1988; Larsen & Furst 2008), cells (Fabry *et al.* 2001; Balland *et al.* 2006), etc., the relaxation modulus decays as $G(t) = St^{-\alpha}$, with the exponent $0 < \alpha < 1$. For such materials, the following form of stress response to an arbitrary shear history needs to be considered (Schiessel *et al.* 1995; Aime *et al.* 2018),

$$\boldsymbol{\sigma}(t) = \frac{E\lambda^{\alpha}}{\Gamma(1-\alpha)} \int_{-\infty}^{t} (t-t')^{-\alpha} \frac{\mathrm{d}\gamma(t')}{\mathrm{d}t'} \mathrm{d}t' \tag{A2}$$

by reformulating the relaxation modulus as $G(t) = (E/(\Gamma(1-\alpha)))(t/\lambda)^{-\alpha}$, where E is a modulus and λ is a characteristic time. In light of the definition of the fractional derivative operator (Caputo type) (Podlubny 1999; Mainardi 2022),

$$\frac{\mathrm{d}^{\alpha}}{\mathrm{d}t^{\alpha}} f(t) = \frac{1}{\Gamma(1-\alpha)} \int_{-\infty}^{t} (t-t')^{-\alpha} \frac{\mathrm{d}f(t')}{\mathrm{d}t'} \mathrm{d}t', \quad 0 < \alpha < 1, \tag{A3}$$

the aforementioned (A2) can be reformulated as

$$\boldsymbol{\sigma}(t) = E\lambda^{\alpha} \frac{\mathrm{d}^{\alpha}\boldsymbol{\gamma}(t)}{\mathrm{d}t^{\alpha}}. \tag{A4}$$

This formalism is commonly referred to as the Scott-Blair element or spring-pot (Scott-Blair *et al.* 1947). The proposed model can be physically implemented via

https://doi.org/10.1017/jfm.2026.12134 Published online by Cambridge University Press

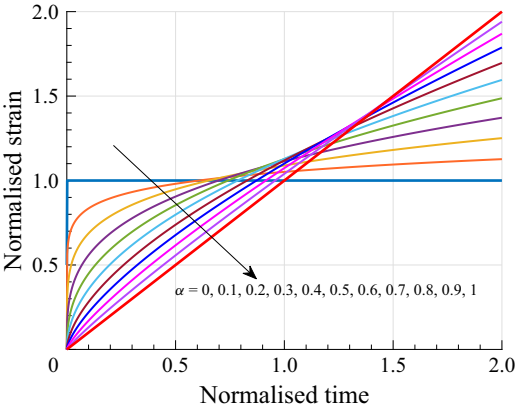


Figure 19. The normalised strain is presented as a function of the normalised time when a constant stress is applied at time $t = 0$ to spring-pots with various exponents α.

hierarchical configurations of springs and dashpots, including ladder-like, tree-like or fractal architectures. Microscopic and mesoscopic interpretations of such continuous viscoelastic structures can be found in Schiessel & Blumen (1995). In the limiting cases of $\alpha = 1$ and $\alpha = 0$, (A4) reduces to the constitutive laws for a viscous Newtonian fluid, $\boldsymbol{\sigma}(t) = \eta(\mathrm{d}\boldsymbol{\gamma}/\mathrm{d}t)$ with $\eta = E\lambda$, and a linear elastic solid, $\boldsymbol{\sigma}(t) = E\boldsymbol{\gamma}$, respectively. For intermediate values of $\alpha \in (0, 1)$, (A4) generalises these behaviours and interpolates between the elastic and viscous extremes. Figure 19 illustrates the interpolation, showing the creep deformation of spring-pot elements with varying fractional exponents α under a step stress applied at $t = 0$.

Analogous to classical integer-order viscoelastic models constructed via the series and parallel combinations of springs and dashpots, spring-pot elements can be used to establish more complex constitutive models. Specifically, two spring-pots, characterised by the parameter pairs (α, E_1, λ_1) and (β, E_2, λ_2), respectively, are connected in series. By assuming stress equivalence across the spring-pots ($\boldsymbol{\sigma} = \boldsymbol{\sigma_1} = \boldsymbol{\sigma_2}$) and strain additivity ($\boldsymbol{\gamma} = \boldsymbol{\gamma_1} + \boldsymbol{\gamma_2}$) , the constitutive equation of the FMM can be systematically derived (Schiessel *et al.* 1995; Tan *et al.* 2003), i.e.

$$\left(1 + \lambda^{\alpha-\beta}\frac{\mathrm{d}^{\alpha-\beta}}{\mathrm{d}t^{\alpha-\beta}}\right)\sigma(t) = E\lambda^{\alpha}\frac{\mathrm{d}^{\alpha}\gamma(t)}{\mathrm{d}t^{\alpha}}, \quad 0 \le \beta \le \alpha \le 1, \tag{A5}$$

where $\lambda = (E_1\lambda_1^{\alpha}/E_2\lambda_2^{\beta})^{1/(\alpha-\beta)}$ and $E = E_1(\lambda_1/\lambda)^{\alpha}$. Without loss of generality, $\alpha > \beta$ is assumed here (Schiessel *et al.* 1995). Friedrich (1991) demonstrated that the model yields non-negative internal work and energy dissipation rate, fulfilling the laws of thermodynamics. It is important to note that the proposed model reduces to the classical integer-order Maxwell model when $\alpha = 1$ and $\beta = 0$. Conversely, when $\alpha = \beta = 1$, the model simplifies to the classical Newtonian fluid model. This special-case analysis not only highlights the versatility of the model but also elucidates its connection with well-established constitutive models in the field of rheology.

In this paper, the experimental data of the viscoelastic storage modulus $G'(\omega)$ and loss modulus $G''(\omega)$ of HEC and XG aqueous solutions are employed. These data are obtained through small-amplitude oscillatory shear deformation tests in the frequency domain. Regarding the FMM, the complex modulus can be analytically derived by applying the

https://doi.org/10.1017/jfm.2026.12134 Published online by Cambridge University Press

Fourier transform to the governing equation (A5):

$$G^* = \frac{E\lambda^\alpha (\mathrm{i}\omega)^\alpha \cdot \lambda^\beta (\mathrm{i}\omega)^\beta}{\lambda^\alpha (\mathrm{i}\omega)^\alpha + \lambda^\beta (\mathrm{i}\omega)^\beta}. \tag{A6}$$

Subsequently, through the separation of the real and imaginary components of the derived equation, the expressions for the storage modulus and loss modulus can be obtained, i.e.

$$G'(\omega) = \frac{E\lambda^\beta \omega^\beta \cos(\pi\alpha/2) + E\lambda^\alpha \omega^\alpha \cos(\pi\beta/2)}{\lambda^{\alpha-\beta}\omega^{\alpha-\beta} + \lambda^{\beta-\alpha}\omega^{\beta-\alpha} + 2\cos(\pi(\alpha-\beta)/2)}, \tag{A7}$$

$$G''(\omega) = \frac{E\lambda^\beta \omega^\beta \sin(\pi\alpha/2) + E\lambda^\alpha \omega^\alpha \sin(\pi\beta/2)}{\lambda^{\alpha-\beta}\omega^{\alpha-\beta} + \lambda^{\beta-\alpha}\omega^{\beta-\alpha} + 2\cos(\pi(\alpha-\beta)/2)}. \tag{A8}$$

When $\alpha = 1$ and $\beta = 0$, expressions (A7) and (A8) simplify to those of the linear Maxwell model, which verifies the consistency between the fractional model and classical theory. The FMM concisely captures the broad spectrum of relaxation dynamics using only four parameters ($\alpha,\ \beta,\ \lambda,\ E$), providing a more parsimonious alternative to traditional models. In contrast, to accurately describe the power-law behaviour of materials by using multiple Maxwell models, an impractically large number of discrete relaxation times is required (Tschoegl 1989).

A.3. *Parameter estimation on polymer solutions*

This subsection focuses on fitting the experimental data for entangled HEC and XG aqueous solutions using the FMM and identifying the model parameters α, β, E and λ via an enhanced differentiated creative search (DCS) algorithm (Duankhan *et al.* 2024). The original DCS algorithm, known for its strong evolutionary and optimisation capabilities, suffers from uneven solution space distribution due to random initialisation. To address this, a logistic chaotic map is employed for population initialisation to improve the algorithm's performance in the parameter identification process:

$$P_{k,d} = L_d + \chi \cdot \mathcal{L}(x_{k,d}, \vartheta) \cdot (U_d - L_d), \quad k = 1, \ldots, N_P;\ d = 1, \ldots, D. \tag{A9}$$

Here $P_{k,d}$ represents the position coordinate of the kth individual in the dth dimension, U_d and L_d represent the lower bound and upper bound, respectively, for the dth dimension, N_p is the population size, χ denotes the chaotic disturbance strength coefficient, which regulates the search range of the chaotic mapping in the solution space, $\mathcal{L}(x_{k,d}, \vartheta)$ represents the logistic map function, whose expression is given by

$$\mathcal{L}(x_{k,d}, \vartheta) = \vartheta x_{k,d}(1 - x_{k,d}), \tag{A10}$$

where ϑ is the control parameter, typically set to $\vartheta = 4$ to ensure the system operates in a full chaos state.

The fitness function and constraint conditions for this problem are given as

$$Fitness(X) = \sqrt{\frac{\sum_{s=1}^{N_s} \left(G'_s - G'_{exp}\right)^2 + \left(G''_s - G''_{exp}\right)^2}{N_s}} + cP, \tag{A11}$$

$$0 < \alpha \leq 1, \quad \beta - \alpha < 0, \quad 0 < E, \quad 0 < \lambda. \tag{A12}$$

Here G'_s and G''_s are the storage and loss moduli of the FMM at the sample points, G'_{exp} and G''_{exp} designate the experimental data of storage and loss moduli of the HEC solution or XG solution, N_s represents the number of sample points, P is the penalty coefficient given

https://doi.org/10.1017/jfm.2026.12134 Published online by Cambridge University Press

M_w	Concentration (wt.%)	α	β	$E(Pa)$	$\lambda(s)$	Fitness
7.2×10^5 g mol^{-1}	2.0	0.8417	0.4110	52.0171	0.0243	0.0162
	4.0	0.7674	0.2908	238.3099	0.0532	0.0140
1.3×10^6 g mol^{-1}	1.0	0.7398	0.2130	44.2188	0.0414	0.0208
	1.5	0.7569	0.2345	66.9383	0.2518	0.0154

Table 2. The parameter estimation results for HEC solutions.

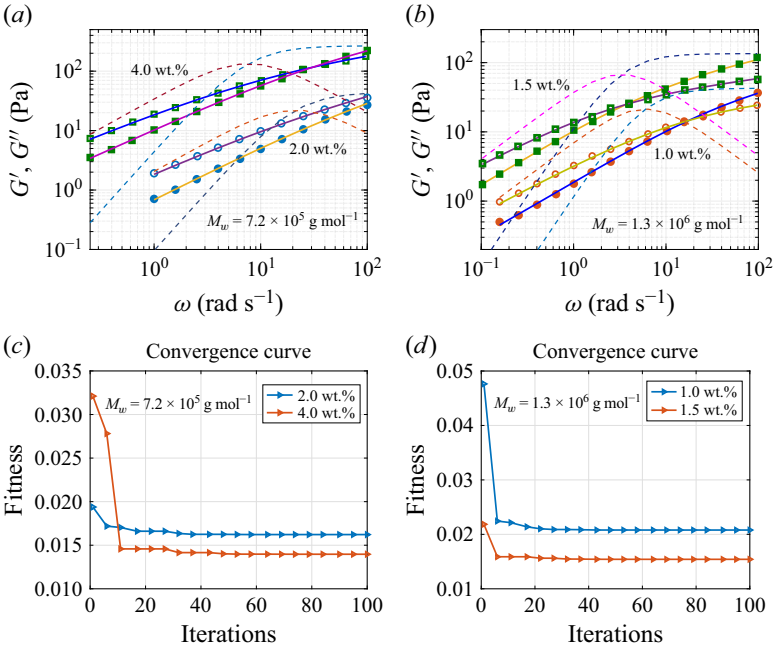


Figure 20. (*a,b*) The fitting results for the storage modulus G' (closed symbols) and loss modulus G'' (open symbols) of HEC solutions in Dinic & Sharma (2020) with the FMM (solid lines) and classical Maxwell model (dashed lines) at $M_w = 7.2 \times 10^5$ g mol^{-1} and $M_w = 1.3 \times 10^6$ g mol^{-1}, respectively. (*c,d*) Iterative convergence curve of parameter inversion for HEC solutions with DCE method.

by a large number (10^5) and c is the number of instances that do not meet the constraint conditions, (α, β, λ, E) is the parameter vector to be estimated.

Using experimental data for the storage and loss moduli of HEC solutions with varying molecular weights (M_w) and concentrations at 5 % strain amplitude (Dinic & Sharma 2020), we determined the parameters of the FMM via the DCS method. The fitting results are presented in figures 20(*a*) and 20(*b*), and estimated parameters are listed in table 2. For comparison, figure 20 also includes the fits obtained with the classical Maxwell model. It is evident that the FMM accurately captures the moduli across the different HEC solutions, whereas the classical Maxwell model exhibits significant deviations. To evaluate the effectiveness of the DCS algorithm, convergence curves of the parameter inversion process are shown in figures 20(*c*) and 20(*d*). The fitness value decreases rapidly within 5–10 iterations and then stabilises, demonstrating both high stability and fast convergence of the algorithm. The corresponding minimum fitness values are detailed in the last column of table 2. To further demonstrate the broad applicability of the FMM, the DCS algorithm

https://doi.org/10.1017/jfm.2026.12134 Published online by Cambridge University Press

Concentration	α	β	$E(Pa)$	$\lambda(s)$	Fitness
0.05 w/w%	0.9798	0.4169	0.0671	9.3457	0.0121
0.1 w/w%	0.9314	0.3684	0.2399	3.3318	0.0148

Table 3. The parameter estimation results for XG aqueous solutions.

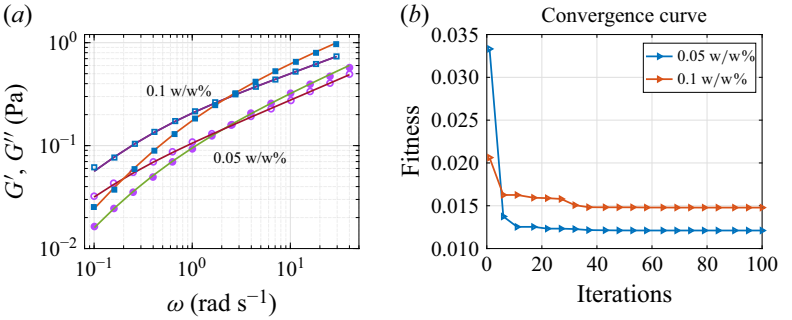


Figure 21. (*a*) The fitting results for the storage modulus G' (closed symbols) and loss modulus G'' (open symbols) of XG aqueous solutions in Cao & Kraume (2022) with the FMM. (*b*) Iterative convergence curve of parameter inversion for XG solution with DCE method.

was applied to fit the storage and loss moduli of XG aqueous solution at 10 % deformation (Cao & Kraume 2022). As shown in figure 21(*a*), the FMM predictions agree excellently with the experimental data. The estimated parameters, listed in table 3, are consistent with theoretical and literature values. Moreover, the convergence behaviour in figure 21(*b*) and the low fitness values in table 3 confirm the algorithm's robustness and stability, affirming both the reliability of the parameters and the effectiveness of the method.

In conclusion, it is imperative to highlight that the FMM not only excellently fits the two polymer solutions studied here but also shows strong versatility across diverse systems, including other polymers (Hu & Zhu 2011; Jaishankar & McKinley 2014; Wagner *et al.* 2017; Ferrás *et al.* 2018), biological solutions (Yang *et al.* 2018) and viscoelastic interfaces (Jaishankar & McKinley 2013). Its ability to capture a wider range of relaxation times compared with classical and multi-mode models highlights the broad applicability and superiority of fractional calculus-based viscoelastic modelling. Furthermore, the capability of fractional calculus to describe complex multi-scale dynamics underscores its broader applicability, with significant potential in fields like turbulent flow modelling (Keith *et al.* 2021; Samiee *et al.* 2022; Akhavan-Safaei & Zayernouri 2023; Barros & Escauriaza 2024).

Appendix B

The coefficients $C_1 - C_4$ and parameter A in (3.21) are given as follows:

$$A = \left(i^{1-\alpha}De^{1-\alpha} + i^{1-\beta}De^{1-\beta}\right)(Rei + Ha^2), \tag{B1}$$

$$B = -\frac{\kappa^2\zeta}{I_0(\kappa)}\left(i^{1-\alpha}De^{1-\alpha} + i^{1-\beta}De^{1-\beta}\right)\left(1 + \kappa\delta\frac{\sinh\zeta}{\zeta}\right), \tag{B2}$$

$$C_1 = \frac{1}{2(A-\kappa^2)[\mathrm{I}_0(\sqrt{A}) + \sqrt{A}\delta\mathrm{I}_1(\sqrt{A})]}, \tag{B3}$$

https://doi.org/10.1017/jfm.2026.12134 Published online by Cambridge University Press

$$C_2 = 2B(\mathrm{I}_0(\kappa) + \delta\kappa \mathrm{I}_1(\kappa)), \tag{B4}$$

$$C_3 = \sqrt{A}B\pi \mathrm{I}_0(\sqrt{A}) + AB\delta\pi \mathrm{I}_1(\sqrt{A}), \tag{B5}$$

$$C_4 = B\kappa\pi \mathrm{I}_0(\sqrt{A}) + \sqrt{A}B\delta\kappa\pi \mathrm{I}_1(\sqrt{A}). \tag{B6}$$

Here parameter A is a comprehensive multi-physical coupling parameter that integrates viscoelastic effects (De, α, β), oscillatory inertia (Re) and magnetic damping (Ha^2). Its magnitude directly governs the radial shape of the velocity profile, reflecting the combined modulation of viscoelasticity, inertia and magnetic forces. Parameter B acts as a correction coefficient for the effective EO driving strength, quantifying the EO force modulated by viscoelasticity and interfacial slip. Coefficients C_1 to C_4 incorporate the electrokinetic parameter κ, slip length δ and parameter A, ensuring that the velocity solution satisfies the wall boundary conditions.

The expression (3.21) can be reformulated into the following equivalent form by means of the regularised confluent hypergeometric function:

$$u_0(r) = N_1 \mathrm{I}_0(\sqrt{A}r) - N_2 \mathrm{I}_0(\kappa r). \tag{B7}$$

Here

$$N_1 = \frac{2N_2\,[\mathrm{I}_0(\kappa) + \kappa\delta \mathrm{I}_1(\kappa)]}{2\mathrm{I}_0(\sqrt{A}) + A\delta\ {}_0F_1\left(;2;\frac{A}{4}\right)}, \tag{B8}$$

$$N_2 = \frac{B}{A-\kappa^2}, \tag{B9}$$

where the two Bessel function terms represent distinct flow modes: $\mathrm{I}_0(\sqrt{A}r)$ captures viscoelastic-magnetic-electro-osmotic interactions, with $\sqrt{A}r$ governing its radial profile; $\mathrm{I}_0(\kappa r)$ is the pure AC electro-osmotic base flow, whose radial structure depends solely on κ. The coefficients N_1 and N_2 weight these two modes, incorporating κ, δ and all key coupling parameters to quantify the contribution of each mechanism to the overall velocity profile. Moreover, this simple expression form will be used when solving the subsequent concentration distribution. Here ${}_0F_1(a;b;z)$ is the regularised confluent hypergeometric function, which is related to the confluent hypergeometric function ${}_0M_1(a;b;z)$ (Brychkov 2008):

$${}_0F_1(a;b;z) = \frac{{}_0M_1(a;b;z)}{\Gamma(b)}. \tag{B10}$$

The confluent hypergeometric function is one of the generalised hypergeometric functions of order m, n, which is defined as

$$\begin{aligned} {}_mM_n(a;b;z) &= {}_m\,M_n(a_1,\ldots,a_j,\ldots,a_m;b_1,\ldots,b_k,\ldots b_n;z) \\ &= \sum_{q=0}^{\infty}\left(\frac{(a_1)_q,\ldots,(a_j)_q,\ldots,(a_m)_q}{(b_1)_q,\ldots,(b_k)_q,\ldots,(b_n)_q}\right)\left(\frac{z^q}{q!}\right), \end{aligned} \tag{B11}$$

where $(a)_q$ and $(b)_q$ are Pochhammer symbols, $a = (a_1, a_2, \ldots, a_m)$ and $b = (b_1, b_2, \ldots, b_n)$ are vectors of lengths m and n, respectively. If a or b is the empty vector,

https://doi.org/10.1017/jfm.2026.12134 Published online by Cambridge University Press

then the hypergeometric function ${}_mM_n(a;b;z)$ can be reduced as

$$
\begin{aligned}
{}_0M_n(;b;z) &= \sum_{q=0}^{\infty}\left(\frac{1}{(b_1)_q,\ldots,(b_k)_q,\ldots,(b_n)_q}\right)\left(\frac{z^q}{q!}\right),\\
{}_mM_0(a;;z) &= \sum_{q=0}^{\infty}\left((a_1)_q,\ldots,(a_j)_q,\ldots,(a_m)_q\right)\left(\frac{z^q}{q!}\right),\\
{}_0M_0(;;z) &= \sum_{q=0}^{\infty}\left(\frac{z^q}{q!}\right)=\mathrm{e}^z.
\end{aligned}
\tag{B12}
$$

Appendix C

Suppose the solution of $g_1(r,t)$ takes the form $g_1(r,t)=\mathrm{Im}\{G(r)\mathrm{e}^{\mathrm{i}\omega t}\}$, then upon substituting this into (3.33*a*) and (3.34*b*) and omitting both the imaginary part and $\mathrm{e}^{\mathrm{i}\omega t}$, the simplified equation and the corresponding boundary conditions are

$$r^2G''(r)+rG'(r)-i\omega r^2G(r)=r^2u_0(r)-r^2U_1, \tag{C1}$$

$$\frac{\mathrm{d}G(0)}{\mathrm{d}r}=\frac{\mathrm{d}G(1)}{\mathrm{d}r}=0. \tag{C2}$$

Equation (C1) is a second-order linear non-homogeneous ordinary differential equation. Its solution can be expressed as the sum of the general solution $G_1(r)$ of the corresponding homogeneous equation and the particular solution $G_2(r)$ of the non-homogeneous equation, i.e. $G(r)=G_1(r)+G_2(r)$. The homogeneous equation that $G_1(r)$ satisfies and the non-homogeneous equation that $G_2(r)$ satisfies are presented as follows:

$$r^2G_1''(r)+rG_1'(r)-i\omega r^2G_1(r)=0, \tag{C3}$$

$$r^2G_2''(r)+rG_2'(r)-i\omega r^2G_2(r)=r^2u_0(r)-r^2U_1. \tag{C4}$$

Equation (C3) is a modified Bessel equation of order 0 and its solution can be directly written out as

$$G_1(r)=A_1\mathrm{I}_0(\sqrt{i\omega}r)+A_2\mathrm{K}_0(\sqrt{i\omega}r), \tag{C5}$$

where I_0 and K_0 are the modified Bessel function of the first kind and second kind zero order, constants A_1 and A_2 are decided by the relevant boundary conditions. In light of the composition of the right-hand side of (C4), the particular solution assumes the following form according to the superposition principle of solutions:

$$G_2(r)=A_3+A_4\mathrm{I}_0(\sqrt{A}r)+A_5\mathrm{I}_0(\kappa r). \tag{C6}$$

Firstly, the $A_3=U_1/i\omega$ can be determined by substituting $G_2=A_3$ into the following equation:

$$r^2G_2''(r)+rG_2'(r)-i\omega r^2G_2(r)=-r^2U_1. \tag{C7}$$

Then, bring $A_4\mathrm{I}_0(\sqrt{A}r)+A_5\mathrm{I}_0(\kappa r)$ into the equation

$$r^2G_2''(r)+rG_2'(r)-i\omega r^2G_2(r)=r^2u_0(r), \tag{C8}$$

we have

$$A_4r^2\left(\mathrm{I}_0\left(\sqrt{A}r\right)\right)''+A_4r\left(\mathrm{I}_0\left(\sqrt{A}r\right)\right)'-A_4i\omega r^2\mathrm{I}_0\left(\sqrt{A}r\right)=r^2N_1\mathrm{I}_0\left(\sqrt{A}r\right), \tag{C9}$$

$$A_5r^2\left(\mathrm{I}_0(\kappa r)\right)''+A_5r\left(\mathrm{I}_0(\kappa r)\right)'-A_5i\omega r^2\mathrm{I}_0\left(\kappa r\right)=-r^2N_2\mathrm{I}_0\left(\kappa r\right). \tag{C10}$$

https://doi.org/10.1017/jfm.2026.12134 Published online by Cambridge University Press

Meanwhile, let $A_4\mathrm{I}_0(\sqrt{A}r)$ and $A_5\mathrm{I}_0(\kappa r)$ be the solutions of the following homogeneous equation, respectively:

$$A_4 r^2\big(\mathrm{I}_0\big(\sqrt{A}r\big)\big)'' + A_4 r\big(\mathrm{I}_0\big(\sqrt{A}r\big)\big)' - A_4 A r^2\mathrm{I}_0\big(\sqrt{A}r\big) = 0, \tag{C11}$$

$$A_5 r^2\,(\mathrm{I}_0(\kappa r))'' + A_5 r\,(\mathrm{I}_0(\kappa r))' - A_5\kappa^2 r^2\mathrm{I}_0\,(\kappa r) = 0. \tag{C12}$$

By solving the above four equations (C9)–(C12), the constants A_4 and A_5 can be determined as

$$A_4 = \frac{N_1}{A - i\omega}, \quad A_5 = -\frac{N_2}{\kappa^2 - i\omega}. \tag{C13}$$

Therefore, the solution of (C1) can be expressed as the following form:

$$G(r) = A_1\mathrm{I}_0\big(\sqrt{i\omega}r\big) + A_2\mathrm{K}_0\big(\sqrt{i\omega}r\big) + A_3 + A_4\mathrm{I}_0\big(\sqrt{A}r\big) + A_5\mathrm{I}_0(\kappa r). \tag{C14}$$

Based on the value of A_3, A_4 and A_5 obtained above, and by means of the boundary conditions, the constants A_1 and A_2 can be deduced as

$$A_1 = -\frac{A_5\kappa\mathrm{I}_1(\kappa) + A_4\sqrt{A}\mathrm{I}_1(\sqrt{A})}{\sqrt{i\omega}\mathrm{I}_1(\sqrt{i\omega})}, \quad A_2 = 0. \tag{C15}$$

Ultimately, the solution of (3.33*a*) can be presented as

$$\begin{aligned} g_1(r,t) &= \mathrm{Im}\big\{G(r)\mathrm{e}^{\mathrm{i}\omega t}\big\} \\ &= \mathrm{Im}\big\{\big[A_1\mathrm{I}_0(\sqrt{i\omega}r) + A_3 + A_4\mathrm{I}_0(\sqrt{A}r) + A_5\mathrm{I}_0(\kappa r)\big]\mathrm{e}^{\mathrm{i}\omega t}\big\}. \end{aligned} \tag{C16}$$

References

Ai, Y.D., Dai, H.C., Zhai, Y.W., Chen, B. & Huai, W.X. 2022 The effect of solute release position on transient solute dispersion in floating wetlands: an analytical study. *J. Clean. Prod.* **369**, 133370.

Aime, S., Cipelletti, L. & Ramos, L. 2018 Power law viscoelasticity of a fractal colloidal gel. *J. Rheol.* **62**, 1429–1441.

Akhavan-Safaei, A. & Zayernouri, M. 2023 A non-local spectral transfer model and new scaling law for scalar turbulence. *J. Fluid Mech.* **956**, A26.

Arcos, J.C., Méndez, F., Bautista, E.G. & Bautista, O. 2018 Dispersion coefficient in an electro-osmotic flow of a viscoelastic fluid through a microchannel with a slowly varying wall zeta potential. *J. Fluid Mech.* **839**, 348–386.

Aris, R. 1956 On the dispersion of a solute in a fluid flowing through a tube. *Proc. R. Soc. Lond. A* **235** (1200), 67–77.

Azari, M. & Sadeghi, A. 2022 Unsteady convective-diffusive transport in semicircular microchannels with irreversible wall reaction. *J. Fluid Mech.* **949**, A1.

Balland, M., Desprat, N., Icard, D., Feriol, S., Asnacios, A., Browaeys, J., Hanon, S. & Gallet, F. 2006 Power laws in microrheology experiments on living cells: comparative analysis and modeling. *Phys. Rev. E* **74**, 021911.

Banerjee, D., Mehta, S.K., Pati, S. & Biswas, P. 2021 Analytical solution to heat transfer for mixed electroosmotic and pressure-driven flow through a microchannel with slip-dependent zeta potential. *Intl J. Heat Mass Transfer* **181**, 121989.

Banerjee, D., Pati, S. & Biswas, P. 2023 Analytical study of pulsatile mixed electroosmotic and shear-driven flow in a microchannel with a slip-dependent zeta potential. *Appl. Math. Mech. -Engl. Ed.* **44** (6), 1007–1022.

Barros, M. & Escauriaza, C. 2024 Lagrangian and Eulerian perspectives of turbulent transport mechanisms in a lateral cavity. *J. Fluid Mech.* **984**, A1.

Bartels, C.F. & Churchill, R.V. 1942 Resolution of boundary problem by the use of a generalized convolution. *Bull. Am. Math. Soc.* **48**, 276–282.

Barton, N.G. 1983 The dispersion of solute from time-dependent releases in parallel flow. *J. Fluid Mech.* **136**, 243–267.

https://doi.org/10.1017/jfm.2026.12134 Published online by Cambridge University Press

BIRD, R.B., STEWART, W.E. & LIGHTFOOT, E.N. 2001 *Transport Phenomena*, 2nd edn. Wiley-Interscience Publication.

BRYCHKOV, Y.A. 2008 *Handbook of Special Functions* CRC Press.

CAO, C. & KRAUME, M. 2022 Improved mixing of viscoelastic fluids by the use of hysteresis effect. *Chem. Engng Sci.* **260**, 11787.

CHAKRABORTY, R., DEY, R. & CHAKRABORTY, S. 2013 Thermal characteristics of electromagnetohydrodynamic flows in narrow channels with viscous dissipation and Joule heating under constant wall heat flux. *Intl J. Heat Mass Transfer* **67**, 1151–1162.

CHATWIN, P.C. 1970 The approach to normality of the concentration distribution of a solute in a solvent flowing along a straight pipe. *J. Fluid Mech.* **43** (2), 321–352.

CHAUDHURI, J., MANDAL, T.K. & BANDYOPADHYAY, D. 2018 Steady and oscillatory Lorentz-force-induced transport and digitization of two-phase microflows. *Phys. Rev. Appl.* **10**, 034057.

CHEN, Y., LI, J., LV, Z.Y., WEI, Y.Q. & LI, C. 2023 Mixing performance of viscoelastic fluids in an induced charge electroosmotic micromixer with a conductive cylinder. *J. Non-Newtonian Fluid Mech.* **317**, 105047.

CHOWDHURY, S., PAL, S.K. & GOPMANDAL, P.P. 2025 Dynamic electroosmotic flow and solute dispersion through a nanochannel filled with an electrolyte surrounded by a layer of a dielectric and immiscible liquid. *Soft Matt.* **21** (6), 1085–1112.

CHURAEV, N.V., RALSTON, J., SERGEEVA, I.P. & SOBOLEV, V.D. 2002 Electrokinetic properties of methylated quartz capillaries. *Adv. Colloid Interface Sci.* **96** (1-3), 265–278.

COLBY, R.H., BORIS, D.C., KRAUSE, W.E. & DOU, S. 2007 Shear thinning of unentangled flexible polymer liquids. *Rheol. Acta* **46**, 569–575.

DAS, C., MONDAL, K.K., PODDAR, N. & WANG, P. 2024*a* Transient dispersion of a reactive solute in an oscillatory Couette flow through an anisotropic porous medium. *Phys. Fluids* **36** (2), 023610.

DAS, D., PODDAR, N. & KAIRI, R.R. 2024*b* Modulating solute transport in magnetohydrodynamic pulsatile electroosmotic micro-channel flow: role of symmetric and asymmetric wall zeta potentials. *Phys. Fluids* **36** (9), 092030.

DAS, D., VAJRAVELU, K. & KAIRI, R.R. 2025 Irreversibility estimation in electroosmotic MHD shear thinning nanofluid flow through a microchannel with slip-dependent zeta potentials. *Chin. J. Phys.* **95**, 118–139.

DEHE, S., REHM, I.S. & HARDT, S. 2021 Hydrodynamic dispersion in Hele–Shaw flows with inhomogeneous wall boundary conditions. *J. Fluid Mech.* **925**, A11.

DENG, S.Y., XIAO, T. & LIANG, C.X. 2024 Analytical study of unsteady two-layer combined electroosmotic and pressure-driven flow through a cylindrical microchannel with slip-dependent zeta potential. *Chem. Engng Sci.* **283**, 119327.

DENTZ, M., ICARDI, M. & HIDALGO, J.J. 2018 Mechanisms of dispersion in a porous medium. *J. Fluid Mech.* **841**, 851–882.

DHELLEMMES, L., LECLERCQ, L., LICHTENAUER, L., HOCHSMANN, A., LEITNER, M., EBNER, A., MICHEL MARTIN, M., NEUSU, C. & COTTET, H. 2024 Dual contributions of analyte adsorption and electroosmotic inhomogeneity to separation efficiency in capillary electrophoresis of proteins. *Anal. Chem.* **96**, 11172–11180.

DINIC, J. & SHARMA, V. 2020 Power laws dominate shear and extensional rheology response and capillarity-driven pinching dynamics of entangled hydroxyethyl cellulose (HEC) solutions. *Macromolecules* **53**, 3424–3437.

DONG, C., ZHANG, J.S., WANG, K. & LUO, G.S. 2014 Micromixing performance of nanoparticle suspensions in a micro-sieve dispersion reactor. *Chem. Engng J.* **253**, 8–15.

DUANKHAN, P., SUNAT, K., CHIEWCHANWATTANA, S. & NASA-NGIUM, P. 2024 The Differentiated Creative Search (DCS): leveraging differentiated knowledge-acquisition and creative realism to address complex optimization problems. *Expert Syst. Appl.* **252**, 123734.

FABRY, B., MAKSYM, G.N., BUTLER, J.P., GLOGAUER, M., NAVAJAS, D. & FREDBERG, J.J. 2001 Scaling the microrheology of living cells. *Phys. Rev. Lett.* **87**, 148102.

FERRY, J.D. 1980 *Viscoelastic Properties of Polymers*. John Wiley & Sons.

FERRÁS, L.L., FORD, N.J., MORGADO, M.L., REBELO, M., MCKINLEY, G.H. & NÓBREGA, J.M. 2018 Theoretical and numerical analysis of unsteady fractional viscoelastic flows in simple geometries. *Comput. Fluids* **174**, 14–33.

FRIEDRICH, C. 1991 Relaxation functions of rheological constitutive equations with fractional derivatives: thermodynamical constraints. In *Rheological Modelling: Thermodynamical and Statistical Approaches. Lecture Notes in Physics* (ed. Casas-Vázquez, J. & Jou, D.), vol. 381, pp. 321–330. Springer.

GHOSAL, S. 2006 Electrokinetic flow and dispersion in capillary electrophoresis. *Annu. Rev. Fluid Mech.* **38**, 309–338.

https://doi.org/10.1017/jfm.2026.12134 Published online by Cambridge University Press

GHOSAL, S. & CHEN, Z. 2012 Electromigration dispersion in a capillary in the presence of electro-osmotic flow. *J. Fluid Mech.* **697**, 436–454.
GILL, W.N. & SANKARASUBRAMANIAN, R. 1970 Exact analysis of unsteady convective diffusion. *Proc. R. Soc. Lond. A* **316** (1526), 341–350.
GILL, W.N. & SANKARASUBRAMANIAN, R. 1971 Dispersion of a non-uniform slug in time-dependent flow. *Proc. R. Soc. Lond. A* **322** (1548), 101–117.
GILL, W.N. & SANKARASUBRAMANIAN, R. 1972 Dispersion of non-uniformly distributed time-variable continuous sources in time-dependent flow. *Proc. R. Soc. Lond. A* **327** (1569), 191–208.
GOYAL, V., DATTA, S. & CHAKRABORTY, S. 2024 Generalizing electroosmotic-flow predictions over charge-modulated periodic topographies: tuneable far-field effects. *J. Fluid Mech.* **990**, A1.
HEGDE, A.S. & HARIKRISHNAN, A.R. 2021 Slip hydrodynamics of combined electroosmotic and pressure driven flows of power law fluids through narrow confinements. *Eur. J. Mech. B Fluids* **89**, 525–550.
HU, K.X. & ZHU, K.Q. 2011 Anote on fractional Maxwell model for PMMA and PTFE. *Polym. Test.* **30** (7), 797–799.
HUANG, S., DEBNATH, S., ROY, A.K., WANG, J., JIANG, W., BEG, O.A. & KUHARAT, S. 2024 Transient dispersion of reactive solute transport in electrokinetic microchannel flow. *Phys. Fluids* **36** (5), 052011.
HUANG, H.F., KUO, J.E. & HUANG, K.H. 2022 Passive solute separation in AC electroosmosis including surface charge-coupled hydrodynamic slip effects. *Electrophoresis* **43** (4), 571–580.
JAISHANKAR, A. & MCKINLEY, G.H. 2013 Power-law rheology in the bulk and at the interface: quasi-properties and fractional constitutive equations. *Proc. R. Soc. A* **469** (2149), 20120284.
JAISHANKAR, A. & MCKINLEY, G.H. 2014 A fractional K-BKZ constitutive formulation for describing the nonlinear rheology of multiscale complex fluids. *J. Rheol.* **58** (6), 1751–1788.
JANG, J. & LEE, S.S. 2000 Theoretical and experimental study of MHD (magnetohydrodynamic) micropump. *Sens. Actuators* **80**, 84–89.
JIMENEZ, C. & SULLIVAN, P.J. 1984 Contaminant dispersion in some time-dependent laminar flows. *J. Fluid Mech.* **142**, 57–77.
JOLY, L., YBERT, C., TRIZAC, E. & BOCQUET, L. 2006 Liquid friction on charged surfaces: from hydrodynamic slippage to electrokinetics. *J. Chem. Phys.* **125** (20), 204716.
KEITH, B., KHRISTENKO, U. & WOHLMUTH, B. 2021 A fractional PDE model for turbulent velocity fields near solid walls. *J. Fluid Mech.* **916**, A21.
KOLLMANNSBERGER, P. & FABRY, B. 2011 Linear and nonlinear rheology of living cells. *Annu. Rev. Mater. Res.* **41**, 75–97.
KUNTAL, Y., GHIYA, N. & TIWARI, A. 2025 Solute dispersion in an electroosmotic flow of Carreau and Newtonian fluids through a tube: analytical study. *Eur. Phys. J. Plus* **140**, 221.
LARSEN, T.H. & FURST, E.M. 2008 Microrheology of the liquid-solid transition during gelation. *Phys. Rev. Lett.* **100**, 146001.
LI, D. 2004 *Electrokinetics in Microfluidics*. Academic Press.
LI, H.C. & JIAN, Y.J. 2017 Dispersion for periodic electro-osmotic flow of Maxwell fluid through a microtube. *Intl J. Heat Mass Transfer* **115**, 703–713.
LI, F.Q. & JIAN, Y.J. 2019 Solute dispersion generated by alternating current electric field through polyelectrolyte-grafted nanochannel with interfacial slip. *Intl J. Heat Mass Transfer* **141**, 1066–1077.
LIAO, H.Z., DASGUPTA, P.K., SRINIVASAN, K. & LIU, Y. 2015 Mixing characteristics of mixers in flow analysis. Application to two-dimensional detection in ion chromatography. *Anal. Chem.* **87** (1), 793–800.
LIU, Q.S., JIAN, Y.J., CHANG, L. & YANG, L.G. 2012 Alternating current (AC) electroosmotic flow of generalized Maxwell fluids through a circular microtube. *Intl J. Phys. Sci.* **7** (45), 5935–5941.
LIU, Y.P., JIAN, Y.J., LIU, Q.S. & LI, F.Q. 2015 Alternating current magnetohydrodynamic electroosmotic flow of Maxwell fluids between two micro-parallel plates. *J. Mol. Liq.* **211**, 784–791.
LIU, Y.B., WU, Z.L. & LIU, G.T. 2024 Electrokinetic energy conversion efficiency in a nanochannel with slip-dependent zeta potential. *Phys. Scr.* **99** (2), 025205.
MAINARDI, F. 2022 *Fractional Calculus and Waves in Linear Viscoelasticity*, 2nd edn. World Scientific.
MARTIN, J.E., ADOLF, D. & WILCOXON, J.P. 1988 Viscoelasticity of near-critical gels. *Phys. Rev. Lett.* **61**, 2620–2623.
MASLIYAH, J.H. & BHATTACHARJEE, S. 2006 *Electrokinetic and Colloid Transport Phenomena*. John Wiley & Sons.
MAZUMDER, B.S. & DAS, S.K. 1992 Effect of boundary reaction on solute dispersion in pulsatile flow through a tube. *J. Fluid Mech.* **239**, 523–549.
MEDEROS, G., ARCOS, J., BAUTISTA, O. & MÉNDEZ, F. 2020 Hydrodynamics rheological impact of an oscillatory electroosmotic flow on a mass transfer process in a microcapillary with a reversible wall reaction. *Phys. Fluids* **32** (12), 122003.

https://doi.org/10.1017/jfm.2026.12134 Published online by Cambridge University Press

MEHTA, S.K. & MONDAL, P.K. 2024 Electroosmotic mixing of viscoplastic fluids in a microchannel. *Phys. Rev. Fluids* **9**, 023301.

MOZAFARI, S., SAFARZADEH, H. & SADEGHI, A. 2025 Analytical solutions for mass transfer and hydrodynamic dispersion by electroosmotic flow of viscoelastic fluids in heterogeneous microchannels. *Intl J. Heat Mass Transfer* **247**, 127165.

MUKHERJEE, S., DASGUPTA, S. & CHAKRABORTY, S. 2020 Temperature-gradient-induced massive augmentation of solute dispersion in viscoelastic micro-flows. *J. Fluid Mech.* **897**, A23.

NGHE, P., TERRIAC, E., SCHNEIDER, M., LI, Z.Z., CLOITRE, M., ABECASSISA, B. & TABELING, P. 2011 Microfluidics and complex fluids. *Lab on a Chip* **11**, 788–794.

PERALTA, M., ARCOS, J., MÉNDEZ, F. & BAUTISTA, O. 2020 Mass transfer through a concentric-annulus microchannel driven by an oscillatory electroosmotic flow of a Maxwell fluid. *J. Non-Newtonian Fluid Mech.* **279**, 104281.

PODDAR, O., SAHA, G., MONDAL, K.K., DHAR, S. & MAZUMDER, B.S. 2024 Effect of phase exchange kinetics on Taylor dispersion of chemically reactive solutes in an oscillatory magnetohydrodynamics flow between two parallel plates. *Phys. Fluids* **36** (5), 053601.

PODLUBNY, I. 1999 *Fractional Differential Equations*. Academic Press.

PONALAGUSAMY, R. & MURUGAN, D. 2023 Transport of a reactive solute in electroosmotic pulsatile flow of non-Newtonian fluid through a circular conduit. *Chin. J. Phys.* **81**, 243–269.

RANA, J. & MURTHY, P.V.S.N. 2016*a* Solute dispersion in pulsatile Casson fluid flow in a tube with wall absorption. *J. Fluid Mech.* **793**, 877–914.

RANA, J. & MURTHY, P.V.S.N. 2016*b* Unsteady solute dispersion in Herschel–Bulkley fluid in a tube with wall absorption. *Phys. Fluids* **28** (11), 111903.

RESHADI, M. & SAIDI, M.H. 2019 Tuning the dispersion of reactive solute by steady and oscillatory electroosmotic-Poiseuille flows in polyelectrolyte-grafted micro/nanotubes. *J. Fluid Mech.* **880**, 73–112.

RILWAN, U.S., ONI, M.O., JHA, B.K. & JIBRIL, H.M. 2024 Analysis of Joule heating and viscous dissipation on electromagnetohydrodynamic flow with electroosmotic effect in a porous microchannel: a heat transfer miniature enhancement. *Heat Transfer* **53** (3), 989–1013.

RUBINSTEIN, I. & ZALTZMAN, B. 2013 Convective diffusive mixing in concentration polarization: from Taylor dispersion to surface convection. *J. Fluid Mech.* **728**, 239–278.

SADEGHI, M., SAIDI, M.H., MOOSAVI, A. & SADEGHI, A. 2020 Unsteady solute dispersion by electrokinetic flow in a polyelectrolyte layer-grafted rectangular microchannel with wall absorption. *J. Fluid Mech.* **887**, A13.

SADR, R., YODA, M., ZHENG, Z. & CONLISK, A.T. 2004 An experimental study of electro-osmotic flow in rectangular microchannels. *J. Fluid Mech.* **506**, 357–367.

SAHA, S. & KUNDU, B. 2022 Electroosmotic pressure-driven oscillatory flow and mass transport of Oldroyd-B fluid under high zeta potential and slippage conditions in microchannels. *Colloid. Surf. A* **647**, 129070.

SAHA, S. & KUNDU, B. 2023 Multi-objective optimization of electrokinetic energy conversion efficiency and entropy generation for streaming potential driven electromagnetohydrodynamic flow of couple stress Casson fluid in microchannels with slip-dependent zeta potentials. *Energy* **284**, 129288.

SAHA, S. & KUNDU, B. 2025 Highest electro-viscous energy and lowest irreversibility analysis for Maxwell fluid in transient microchannel flow. *Appl. Therm. Engng* **267**, 125764.

SAHORE, V., DOONAN, S.R. & BAILEY, R.C. 2018 Droplet microfluidics in thermoplastics: device fabrication, droplet generation, and content manipulation using integrated electric and magnetic fields. *Anal. Methods* **10** (35), 4264–4274.

SAMIEE, M., AKHAVAN-SAFAEI, A. & ZAYERNOURI, M. 2022 Tempered fractional LES modeling. *J. Fluid Mech.* **932**, A4.

SAMUEL, C.J., CHANG, R., MA, K. & SANTIAGO, J.G. 2025 Taylor dispersion for coupled electroosmotic and pressure-driven flows in all time regimes. *J. Fluid Mech.* **1011**, A36.

SANKARASUBRAMANIAN, R. & GILL, W.N. 1972 Dispersion from a prescribed concentration distribution in time variable flow. *Proc. R. Soc. Lond. A* **329** (1579), 479–492.

SANKARASUBRAMANIAN, R. & GILL, W.N. 1973 Unsteady convective diffusion with interphase mass transfer. *Proc. R. Soc. Lond. A* **333** (1592), 115–132.

SCHIESSEL, H. & BLUMEN, A. 1995 Mesoscopic pictures of the sol–gel transition: ladder models and fractal networks. *Macromolecules* **28**, 4013–4019.

SCHIESSEL, H., METZLER, R., BLUMEN, A. & NONNENMACHER, T.F. 1995 Generalized viscoelastic models: their fractional equations with solutions. *J. Phys. A: Math. Gen.* **28**, 6567–6584.

SCHULZ, R., GÄRTTNER, S. & RAY, N. 2024 Investigations of effective dispersion models for electroosmotic flow with rigid and free boundaries in a thin strip. *Math. Meth. Appl. Sci.* **47**, 206–228.

https://doi.org/10.1017/jfm.2026.12134 Published online by Cambridge University Press

SCOTT-BLAIR, G.W., VEINOGLOU, B.C. & CAFFYN, J.E. 1947 Limitations of the Newtonian time scale in relation to non-equilibrium rheological states and a theory of quasi-properties. *Proc. R. Soc. Lond. A* **189** (1016), 69–87.

SEN, R., MONDAL, K.K. & KAIRI, R.R. 2025 Electroosmotic magnetohydrodynamics-driven solute dispersion in couple stress fluid flow through microchannel: effect of transverse electric field. *Phys. Fluids* **37** (2), 023138.

SHATROV, V. & GERBETH, G. 2010 Marginal turbulent magnetohydrodynamic flow in a square duct. *Phys. Fluids* **22** (8), 084101.

SIVA, T., DUBEY, D. & JANGILI, S. 2024 Rotational flow dynamics of electroosmotic transport of couple stress fluid in a microfluidic channel under electromagnetohydrodynamic and slip-dependent zeta potential effects. *Phys. Fluids* **36** (9), 092006.

SIVA, T., JANGILI, S. & KUMBHAKAR, B. 2023 Entropy generation on EMHD transport of couple stress fluid with slip-dependent zeta potential under electrokinetic effects. *Intl J. Therm. Sci.* **191**, 108339.

SOONG, C.Y., HWANG, P.W. & WANG, J.C. 2010 Analysis of pressure-driven electrokinetic flows in hydrophobic microchannels with slip-dependent zeta potential. *Microfluid Nanofluid.* **9**, 211–223.

SPARKS, D., SMITH, R., STRAAYER, M., CRIPE, J., SCHNEIDER, R., CHIMBAYO, A., ANASARI, S. & NAJAFI, N. 2003 Measurement of density and chemical concentration using a microfluidic chip. *Lab on a Chip* **3**, 19–21.

SUBUDHI, D., JANGILI, S. & BARIK, S. 2024 Unsteady solute dispersion of electro-osmotic flow of micropolar fluid in a rectangular microchannel. *Phys. Fluids* **36** (7), 073114.

SUJITH, T., MEHTA, S.K. & PATI, S. 2025 Steric effect induced heat transfer characteristics of electromagnetohydrodynamic electroosmotic flow through a microchannel considering interfacial slip. *Phys. Fluids* **37** (5), 052009.

TAN, W.C., PAN, W.X. & XU, M.Y. 2003 A note on unsteady flows of a viscoelastic fluid with the fractional Maxwell model between two parallel plates. *Intl J. Non-Linear Mech.* **38** (5), 645–650.

TANDON, V. & KIRBY, B.J. 2008 Zeta potential and electroosmotic mobility in microfluidic devices fabricated from hydrophobic polymers: 2. Slip and interfacial water structure. *Electrophoresis* **29** (5), 1102–1114.

TAYLOR, G. 1953 Dispersion of soluble matter in solvent flowing slowly through a tube. *Proc. R. Soc. Lond. A* **219** (1137), 186–203.

THOMPSON, P.A. & TROIAN, S.M. 1997 A general boundary condition for liquid flow at solid surfaces. *Nature* **389** (6649), 360–362.

TSCHOEGL, N.W. 1989 *The Phenomenological Theory of Linear Viscoelastic Behavior*. Springer.

VARGAS, C., ARCOS, J., BAUTISTA, O. & MÉNDEZ, F. 2017 Hydrodynamic dispersion in a combined magnetohydrodynamic-electroosmotic-driven flow through a microchannel with slowly varying wall zeta potentials. *Phys. Fluid* **29** (9), 092002.

VARGAS, C., MÉNDEZ, F., DOCOSLIS, A. & ESCOBEDO, C. 2023 Colloid transport by an oscillatory electroosmotic flow between microelectrodes of axially variable shape. *Phys. Fluids* **35** (9), 092014.

VASISTA, K.N., MEHTA, S.K. & PATI, S. 2022 Electroosmotic mixing in a microchannel with heterogeneous slip dependent zeta potential. *Chem. Engng Process.* **176**, 108940.

VASISTA, K.N., MEHTA, S.K., PATI, S. & SARKAR, S. 2021 Electroosmotic flow of viscoelastic fluid through a microchannel with slip-dependent zeta potential. *Phys. Fluids* **33** (12), 123110.

VEDEL, S. & BRUUS, H. 2012 Transient Taylor-Aris dispersion for time-dependent flows in straight channels. *J. Fluid Mech.* **691**, 95–122.

WAGNER, C.E., BARBATI, A.C., ENGMANN, J., BURBIDGE, A.S. & MCKINLEY, G.H. 2017 Quantifying the consistency and rheology of liquid foods using fractional calculus. *Food Hydrocoll.* **69**, 242–254.

WANG, S., HUANG, X. & YANG, C. 2011 Mixing enhancement for high viscous fluids in a microfluidic chamber. *Lab on a Chip* **11**, 2081–2087.

WANG, M. & KANG, Q. 2010 Modeling electrokinetic flows in microchannels using coupled lattice Boltzmann methods. *J. Comput. Phys.* **229** (3), 728–744.

WANG, X.P., XU, H.Y. & QI, H.T. 2023 Mixing performance of an expansive mixer on viscoelastic solutions under alternating current electric field. *Phys. Fluids* **35** (10), 103109.

WATSON, G.N. 1995 *A Treatise on the Theory of Bessel Functions*, 2nd edn. Cambridge University Press.

WU, Z. & CHEN, G.Q. 2014 Approach to transverse uniformity of concentration distribution of a solute in a solvent flowing along a straight pipe. *J. Fluid Mech.* **740**, 196–213.

XIE, Z.Y. & JIAN, Y.J. 2017 Entropy generation of two-layer magnetohydrodynamic electroosmotic flow through microparallel channels. *Energy* **139**, 1080–1093.

YANG, C., JIAN, Y., XIE, Z. & LI, F. 2019 Heat transfer characteristics of magnetohydrodynamic electroosmotic flow in a rectangular microchannel. *Eur. J. Mech. B Fluid* **74**, 180–190.

https://doi.org/10.1017/jfm.2026.12134 Published online by Cambridge University Press

YANG, J. & KWOK, D.Y. 2002 A new method to determine zeta potential and slip coefficient simultaneously. *J. Phys. Chem. B* **106**, 12851–12855.

YANG, X., QI, H.T. & JIANG, X.Y. 2018 Numerical analysis for electroosmotic flow of fractional Maxwell fluids. *Appl. Math. Lett.* **78**, 1–8.

ZHANG, T., *et al.* 2025 Active microfluidic platforms for particle separation and integrated sensing applications. *ACS Sens.* **10** (8), 5299–5313.

ZHU, Y.X. & GRANICK, S. 2001 Rate-dependent slip of Newtonian liquid at smooth surfaces. *Phys. Rev. Lett.* **87** (9), 096105.

ZHU, Y.X. & GRANICK, S. 2002 Limits of the hydrodynamic no-slip boundary condition. *Phys. Rev. Lett.* **88** (10), 106102.

https://doi.org/10.1017/jfm.2026.12134 Published online by Cambridge University Press